Journal of Structural Geology 213 (2026) 105846



Contents lists available at ScienceDirect

Journal of Structural Geology

journal homepage: www.elsevier.com/locate/jsg





Paleofluid systems and depth-temperature-deformation-time paths of fractured Mesozoic carbonate reservoirs in Provence (SE France) : insights from the multi-proxy geochemical-tectonic analysis of mineralized mesostructures

Olivier Lacombe [a,*], Nicolas E. Beaudoin [b], Anies Zeboudj [a], Juliette Lamarche [c,1], Jean-Paul Callot [b], Laurent Emmanuel [a], Mathieu Daeron [d], Nicolas Espurt [e], Sidonie Revillon [f]

[a] Sorbonne Université, CY Cergy Paris Université, CNRS-INSU, Institut des Sciences de la Terre Paris, ISTeP, Paris, France
[b] Laboratoire des Fluides Complexes et de leurs Réservoirs, Universite de Pau et des Pays de L'Adour, LFCR, E2S-UPPA, CNRS, Pau, France
[c] Aix-Marseille Universite, CNRS, IRD, INRAE, CEREGE, Aix en Provence, France
[d] Laboratoire des Sciences du Climat et de l'Environnement, LSCE/IPSL, UMR 8212 CEA-CNRS-UVSQ, Université Paris-Saclay, France
[e] Université Côte d'Azur, CNRS, Observatoire de la Côte d'Azur, IRD, GEOAZUR, France
[f] SEDISOR, Plouzané, France

A B S T R A C T

The geochemical characterization of syn-kinematic calcite associated with structures formed during the evolution of carbonate reservoirs can provide quantitative constraints on their depth–temperature–deformation–time (depth–T–d–t) paths, provided that structural and temporal frameworks are well established. Here, we propose a novel multi-proxy approach to reconstruct the depth-T-d-t evolution of Late Jurassic to Late Cretaceous carbonate 'reservoir' rocks exposed in several compressional structures in the Provence fold-and-thrust belt. First, analyses of stable oxygen and carbon isotopes, clumped isotopes and radiogenic strontium isotopes of syn-kinematic calcite from a wide spectrum of structures (large-scale thrusts, veins, mesoscale faults, and stylolite jogs) are used to reconstruct the origin and temperature of mineralizing fluids. Our results point to a significant imprint of meteoric water during the 'mid'-Cretaceous Durancian uplift and associated extensional deformation, whereas the fluid system appears to have remained semi-closed during the Late Cretaceous–Eocene Pyrenean shortening, with mixing between marine and meteoric fluids. Second, syn-kinematic calcite precipitated from fluids at (nearly) thermal equilibrium with the host rock are used to constrain the geothermal temperature of the host rocks at specific stages of deformation, while organic-matter pyrolysis and inversion of bedding-parallel stylolite roughness constrain maximum burial temperatures and minimum burial depths, respectively.

Integrating these new depth-T constraints with the sequence of structural development as constrained by published paleostress reconstructions and U–Pb calcite geochronology reveals depth–T–d–t paths that differ substantially from previously published subsidence–uplift histories derived from cross-section restoration. In particular, Tithonian strata in the Mirabeau anticline and Barremian strata in the Nerthe massif experienced significantly greater burial and erosional exhumation during the Durancian uplift and/or the Pyrenean shortening than previously estimated. Our new approach directly constrains both the depth and timing of deformation, providing new insights into the tectono-sedimentary evolution of Provence as well as a transferable framework for reconstructing the burial and deformation histories of carbonate reservoir rocks worldwide.

1. Introduction

Fractured carbonate reservoirs record complex histories of burial, fluid–rock interaction, and deformation controlling present-day porosity, permeability, and connectivity. Reservoir rocks often host multiple generations of mineralized mesostructures, e.g., stylolites, veins, and faults, that impede or enhance fluid flow while archiving evolving stress, temperature, and fluid regimes (e.g., Lacombe and Rolland, 2016; Agosta et al., 2016; Lacombe et al., 2022). Quantitative reconstruction of fracturing history, together with burial and

This article is part of a special issue entitled: A tribute to Juliette Lamarche published in Journal of Structural Geology.

* Corresponding author.
E-mail address: olivier.lacombe@sorbonne-universite.fr (O. Lacombe).

[1] The authors dedicate this work to their colleague and friend Juliette Lamarche, who sadly passed away in the course of acquisition of the data presented in this paper. Her scientific guidance, contribution and commitment to this study are gratefully acknowledged.

https://doi.org/10.1016/j.jsg.2026.105846
Received 11 July 2026; Received in revised form 8 October 2026; Accepted 22 October 2026
Available online 23 October 2026
0191-8141/© 2026 The Authors. Published by Elsevier Ltd. This is an open access article under the CC BY license (http://creativecommons.org/licenses/by/4.0/).

fluid-flow evolution, is central to basin analysis, reservoir quality prediction, and assessing subsurface storage, caprock integrity, and production potential.

Fracturing conditions of carbonate reservoirs are typically reconstructed via microstructural and petrographic-geochemical analyses of host rocks and fractures (e.g., Di Cuia et al., 2005; Hooker et al., 2012; Vitale et al., 2012; Lamarche et al., 2012; Lavenu et al., 2013, 2014; Lavenu and Lamarche, 2018; La Bruna et al., 2020; Manniello et al., 2022), or via mechanical loading-fracturing path modeling (e.g., Petit et al., 2022). These approaches show most fractures form during syn- or post-burial tectonic or fluid overpressure events (e.g., Ahmadhadi et al., 2008; Beaudoin et al., 2014, 2018, 2020a; Gasparrini et al., 2021; Jiang et al., 2025; Zhang et al., 2024). However, background fractures can initiate during early burial and compaction with minimal overpressure while the material is already compacted but still has low cohesion (Berra and Carminati, 2012; Lamarche et al., 2012; Lavenu et al., 2013; Petit et al., 2022), indicating that primary sedimentary facies and diagenesis control brittleness and mechanical layering of, for instance, platform carbonates (Barbier et al., 2012; Lavenu and Lamarche, 2018). Some early fractures may persist and reactivate later, inhibiting the formation of new fractures (Sassi et al., 2012; Lavenu et al., 2013).

Deformation and diagenesis are intimately linked from the early burial to the late exhumation stages of the evolution of sedimentary basins. In the diagenetic domains, i.e., at depths of ~1–10 km and temperatures up to 300°C, brittle and pressure-solution structures in carbonates are not simple passive responses to stress but are active sites of mass transfer, porosity modification, and cementation. Faults, veins and stylolites localize deformation, channel or impede flow, and accommodate pressure-solution and mineral precipitation, feeding back into rock strength (Laubach et al., 2010, 2019). Because they control reservoir-scale fluid flow and mechanics, mineralized mesostructures are prime targets for linking basin burial, deformation timing and conditions, and the evolution of local or basin-scale fluid sources, compositions and temperatures (Beaudoin et al., 2022).

Indeed, calcite mineralization geochemistry constrains fluid sources, compositions, and temperatures during deformation. Stable oxygen ($\delta^{18}O$) and carbon ($\delta^{13}C$) isotopes may record successive fluid pulses from formational fluids to externally derived basinal or hydrothermal fluids linked to tectonic stages, and allow tracking of mixing between the various fluid sources and quantifying degrees of fluid–rock interaction (see review in Beaudoin et al., 2022). Clumped isotope (Δ_{47}) thermometry estimates absolute calcite formation temperatures and fluid $\delta^{18}O$ values, overcoming traditional $\delta^{18}O$ measurement limits. This technique reveals whether calcite precipitated from geothermal fluids, i.e., in thermal equilibrium with the host rock, or from out-of-equilibrium hydrothermal fluids, even at shallow depths (Brigaud et al., 2020; Beaudoin et al., 2020a; MacDonald et al., 2019, 2024). Strontium isotopes further trace fluid sources against the global marine curve (McArthur et al., 2012); near-marine $^{87}Sr/^{86}Sr$ values indicate local seawater remobilization, while more radiogenic signatures reflect fluid interactions with basement or siliciclastic rocks (Beaudoin et al., 2011; Cruset et al., 2018; Muñoz-López et al., 2022; Smeraglia et al., 2020). When integrated with structural observations, geochemical signatures reveal the spatial-temporal evolution of fluid nature and pathways within the evolving stress field. In situ LA-ICP-MS U–Pb geochronology of syn-kinematic calcite provides the absolute timing to link mineralization and fracturing to burial, fluid flow, and regional tectonics. Recently, combining clumped isotope thermometry or fluid inclusion thermo-barometry with U–Pb geochronology has successfully reconstructed fracture development stages relative to thermal-burial and fluid pressure history of sedimentary basins and/or the timing of hydrocarbon migration and accumulation (Mangenot et al., 2017, 2018; Salih et al., 2019; Hoareau et al., 2021; Zhang et al., 2024; Ni et al., 2025; Cong et al., 2022; Su et al., 2022; Cruset et al., 2021; Chen et al., 2022; Yuan et al., 2024; Fattah et al., 2025; Gasparrini et al., 2025).

However, independent reconstructions of depth, temperature (T), and deformation (d) through time (t) in fractured carbonate reservoirs are complex and truly integrated quantitative reconstructions of depth–T–d–t paths remain rare. In continuously subsiding basins the burial-time evolution can be reliably reconstructed using the thickness of the sedimentary column by assuming deformation timing and amount of rock compaction. In fold-and-thrust belts (FTBs), solving simultaneously for temperature and depth is harder because rock uplift and erosion of a given thickness of rocks affect estimates of the past geothermal gradient (Roure et al., 2010; Naeser and McCulloh, 2012; Tissot et al., 1987; Yalcin et al., 1997; Beaudoin and Lacombe, 2018). Organic matter maturity (e.g., vitrinite reflectance, thermometry based on organic matter pyrolysis, RSCM) and low-temperature thermochronology can be used to assess burial depth and exhumation, but require geothermal gradient assumptions and lack a direct link to either specific (meso)structures or to time. Primary fluid inclusion thermometry can provide constraints on depth and timing if reliable burial models exist and/or the host mineral can be dated by geochronology. Only combined aqueous and oil-inclusion thermometry can independently constrain entrapment pressure and temperature of the fluid (Pironon and Bourdet, 2008).

Using stylolites as stress gauges offers an emerging approach to quantify burial depth independently of past geothermal gradients (Beaudoin and Lacombe, 2018). Stylolites are pervasive pressure-solution surfaces in carbonates, which exemplify the coupling between stress, dissolution, and roughening along bedding interfaces. Their morphology, scaling and cross-cutting relationships reveal stress orientations, relative timing and compaction intensity (Stockdale, 1922; Arthaud and Mattauer, 1969; Rispoli, 1981; Petit and Mattauer, 1995; Benedicto and Schultz, 2010; Tavani et al., 2015; Toussaint et al., 2018; Koehn et al., 2007, 2012, 2016, 2022). Beyond the use of bedding-parallel sedimentary stylolites (BPS) as compaction markers, their roughness properties can be related to the magnitude of the vertical stress and, by extension, to the depth of active pressure solution (Schmittbuhl et al., 2004; Ebner et al., 2009; Toussaint et al., 2018). While individual BPS cease developing at varying depths (Zeboudj et al., 2025a), a BPS population develops continuously during burial, so BPS can be used as quantitative indicators for active compaction depth ranges. This approach has been successfully applied to various sedimentary basins (Rolland et al., 2014; Bertotti et al., 2017; Beaudoin et al., 2019, 2020b; Zeboudj et al., 2023; Bah et al., 2023a,b; Bah et al., 2024) and fold-and-thrust belts (Beaudoin et al., 2016, 2025; Labeur et al., 2021, 2024). Nevertheless, stylolite-based depth inversion has not yet been integrated into comprehensive reconstructions tracking both temperature (Beaudoin et al., 2025) and deformation timing. Although pressure solution was previously undatable, recent U–Pb dating of calcite jogs associated with stylolites overcomes this limitation. Jogs are localized zones of calcite precipitation between the tips of two stylolites, that accommodate local displacement perpendicular to the stylolite planes (Aharonov and Karcz, 2019; Beaudoin et al., 2025). Dating calcite in these jogs therefore constrains the active pressure-solution period along the stylolites (Zeboudj et al., 2025a, 2025b).

This brief review highlights the need for a new approach integrating structural, geochemical, and geochronological datasets to determine when and under what physical conditions (depth, T) mineralized fractures formed and to constrain depth–T–d–t paths of their host rocks. This contribution introduces an original workflow combining: (1) sedimentary stylolite roughness inversion for active pressure-solution depth; (2) stable O and C, clumped and radiogenic Sr isotopes in calcite for fluid temperature and origin; (3) host rock organic matter maturity for maximum burial temperature checkpoints; and (4) U–Pb geochronology paired with paleostress analyses for absolute deformation timing and stress regimes. This workflow is tested in the Provence fold-and-thrust belt (SE France) which features a 1500–8000 m thick Mesozoic–Cenozoic carbonate and marl succession with thrust and

mesostructure timing constrained by recent U–Pb dating (Zeboudj et al., 2025a, 2025b). We reconstruct, for the first time, the evolution of past fluid systems during the main stages of the geological history of Provence, including the nature and temperature of the mineralizing fluids and the extent of fluid–rock interaction. We then identify structures containing dated syn-kinematic calcite of which the mineralizing fluid was sufficiently close to thermal equilibrium with the host rock for fluid temperature to provide reliable constraint on rock thermal conditions at a specific stage of deformation. These temperature constraints are integrated with the other available structural, geochemical and burial-depth constraints to quantitatively reconstruct the depth–T–d–t trajectories of the carbonate reservoirs of interest. Beyond challenging and refining regional geological models, this study provides a transferable test case for linking deformation, geochemical processes, fluid flow and basin evolution within a fully time- and depth-calibrated framework.

2. Geological setting

The Provence FTB is located in SE France and consists of the eastern prolongation of the Pyrenean domain. The main structures are E-W striking folds and thrusts, extensional basins, and NNE-SSW to NE-SW striking strike-slip faults (Fig. 1).

2.1. Meso-Cenozoic sedimentary succession of Provence

The deformed sedimentary succession of Provence comprises a variety of rocks including shales, carbonates, sandstones, marls and evaporites. Following deposition of basal sandstones and limestones interbedded with Triassic evaporites, the Tethyan margin subsided throughout the Jurassic and Early Cretaceous, leading to the accumulation of thick marine carbonate successions, including up to 400 m of platform limestones (rudist-rich Urgonian facies) from the Valanginian to the Early Aptian (Masse and Philip, 1976; Léonide et al., 2007; Masse et al., 2009). During the Albian–Cenomanian, the Provence basin was uplifted and emerged above sea level. This so-called Durancian uplift was accompanied by widespread karst bauxite deposits indicative of periods of subaerial exposure and continental weathering (Masse and Philip, 1976; Combes, 1990; Guyonnet-Benaize, 2011; Mondillo et al., 2025) (Fig. 1). The Late Cretaceous–Eocene succession is dominated by continental siliciclastic and carbonate deposits, including organic-rich black limestones of latest Santonian–early Campanian age and lacustrine to fluvial limestones, claystones and sandstones from the Campanian to Maastrichtian. These deposits are locally interbedded with syntectonic breccias recording successive stages of fold growth during the Pyrenean shortening (Leleu et al., 2009). Southeasternmost Provence was largely unaffected by the Durancian uplift, preserving marine conditions and the deposition of rudist-bearing shallow-marine limestones during the Late Cretaceous (Philip, 1972). The Oligocene

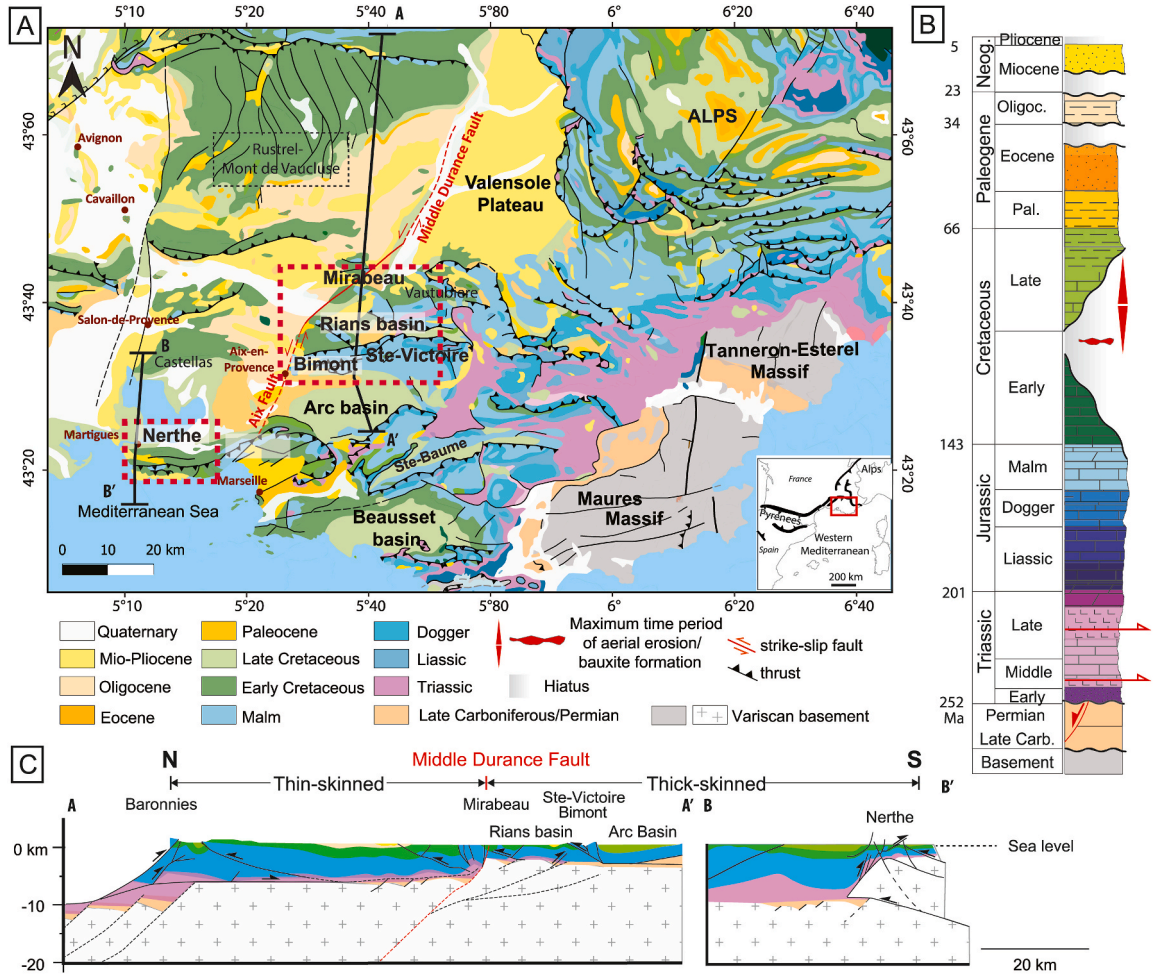


Fig. 1. A : Simplified geological map of the southeastern part of France, modified from Zeboudj et al. (2025a),b. Red frames represent the location of the areas investigated. Black lines represent the location of the composite cross section. Insert shows the map in the setting of the Pyrenees-Provence domain. B: Regional stratigraphic column. C: Crustal-scale cross-section highlighting the main studied structures and the different structural styles, modified after Bestani et al. (2016). (For interpretation of the references to color in this figure legend, the reader is referred to the Web version of this article.)

West-European Rifting (WER) event led to the formation of extensional basins, including the Aix-en-Provence and Marseille basins, which were filled with lacustrine limestones and fluvial conglomerates and shales (Hippolyte et al., 1993). During the Miocene, a marine transgression deposited the so-called 'molasse', consisting of marls and sands (Besson, 2005 and references therein), unconformably overlying the folded Cretaceous and Jurassic units.

2.2. Meso-Cenozoic tectonic, thermal and denudation histories of Provence

The structure of the Provence FTB results from a Mesozoic-Cenozoic polyphase tectonic history made of alternating extensional and contractional tectonic events (Guieu and Roussel, 1990; Gaviglio and Gonzales, 1987; Tempier, 1987; Lacombe et al., 2012; Espurt et al., 2012; Bestani et al., 2016).

From the Triassic to the Early Cretaceous, the Provence domain formed part of the passive continental margin bordering the Tethys Ocean (Dercourt et al., 2000). During the Albian–Cenomanian, divergent movements along the eastern edge of the Iberia–Eurasia plate boundary (Tavani et al., 2018) generated the Durancian uplift, expressed as extensional crustal doming (Masse and Philip, 1976; Guyonnet-Benaize, 2011) (Fig. 1). This doming, associated with roughly E–W-striking normal faults and related horst and graben systems (Aubert et al., 2019), resulted in regional erosion and truncation of strata down to the Late Jurassic limestones. Subaerial exposure promoted karst development and bauxite formation through continental weathering (Mondillo et al., 2025), and led to the development of a Late Cretaceous regional unconformity. Bauxite deposits are overlain by Cenomanian to Campanian–Maastrichtian formations. Geometric reconstructions of the erosional surface and restoration of stratigraphic isopachs indicate 200–800 m of average erosion, locally reaching 1500 m near the axis of the Durancian high, approximately located beneath the Alpilles and Luberon areas (Molliex, 2009; Bruna et al., 2013). There, Early Cretaceous strata were completely removed, locally exposing and incising the Late Jurassic limestones, with a low denudation rate of ~0.01–0.02 mm/yr. In contrast, recent thermochronological data from the Maures–Tanneron Massif, south of the Durancian high, including zircon fission-track (ZFT), apatite fission-track (AFT), and apatite (U–Th–Sm)/He analyses, indicate a Cretaceous heating event between 120 and 75 Ma. This event was interpreted as resulting from crustal thinning and sedimentary burial associated with pre-Pyrenean rifting in the extended domains surrounding the Durancian high, the pre-Pyrenean rift to the south and the Vocontian-Valaisan rift to the north (Boschetti et al., 2025).

From the Campanian until the late Eocene (Bartonian), the NW-SE convergence of the African and Eurasian plates (Dercourt et al., 1986) resulted in the collision of the Iberian plate and the Corsica-Sardinia block with Eurasia (Arthaud and Seguret, 1981; Tempier, 1987; Olivet, 1996; Vergés et al., 2002; Rosenbaum et al., 2002; Lacombe and Jolivet, 2005; Schettino and Turco, 2011; Advokaat et al., 2014; Mouthereau et al., 2014; Grool et al., 2018; Tavani et al., 2018; van Hinsbergen et al., 2020; Angrand and Mouthereau, 2021). This so-called Pyrenean-Provencal shortening produced E-W trending folds and thrusts (Guieu, 1967; Tempier, 1987; Champion et al., 2000; Tempier and Durand, 1981; Séranne et al., 1995; Andreani et al., 2010; Espurt et al., 2012; Lavenu et al., 2013; Bestani et al., 2016), such as the Mirabeau, Bimont and Nerthe fold structures investigated in this study, as well as left-lateral strike-slip faults striking NNE–SSW to NE–SW like the Aix-Middle Durance Fault (AMDF) system. The Pyrenean-Provencal stress regime was either compressional or strike-slip in type, with the maximum principal stress (σ_1) oriented approximately N-S on a regional scale (Bergerat, 1987; Gaviglio and Gonzales, 1987; Lacombe et al., 2012), with variations from NNE–SSW (Balansa et al., 2022) to NNW–SSE (Andreani et al., 2010; Espurt et al., 2012). Erosion during this contractional phase was heterogeneous but substantial. AFT ages clustering around 60 Ma in the Maures Massif, where the pre-Triassic basement crops out, have been interpreted as evidence of tectonically driven uplift and denudation related to the Pyrenean shortening (Jakni, 2000). In the Maures–Tanneron Massif, a regional cooling event beginning at ~75–70 Ma and continuing until ~40 Ma has likewise been attributed to Pyrenean shortening, denudation and exhumation (Boschetti et al., 2025). Thermal inversion models indicate cooling from temperatures consistent with Mesozoic burial depths of ~2–4 km in the Maures and ~1.5 km in the Tanneron, depending on the assumed geothermal gradient (Boschetti et al., 2025). These values correspond to mean denudation rates of ~0.07–0.1 mm/yr in the Maures and ~0.03–0.04 mm/yr in the Tanneron during Pyrenean exhumation. These rates are consistent with the influx of crystalline detritus recorded in Eocene conglomerates and sands of the Basse-Provence basins. Estimates of the volume of these syn-orogenic deposits suggest that surrounding feeder reliefs, such as the Sainte-Victoire and Etoile massifs, may have reached elevations of 1500–2000 m during the Paleocene–Eocene, compared with present-day residual elevations of ~1000 and ~800 m, respectively. Much of this erosion contributed to the formation of a widespread Eocene–Oligocene planation surface (Bestani et al., 2015, 2016; Espurt et al., 2012).

From the latest Eocene (Priabonian) to the Oligocene, E–W extension associated with West-European Rifting (WER) led to the formation of the Aix-en-Provence (Gaviglio and Gonzales, 1987; Espurt et al., 2012), Manosque (Roure and Colletta, 1996) and Marseille (Hippolyte et al., 1993) basins, as well as other basins in Languedoc (Séranne et al., 2021). This phase was followed during the Oligo–Aquitanian by the Liguro-Provençal Rifting (LPR) and the counterclockwise rotation of the Corsica–Sardinia block, driven by trench retreat and African slab rollback (Faccenna et al., 1997, 2003; Gueguen et al., 1998; Lacombe and Jolivet, 2005; Gattacceca et al., 2007, 2008; Cherchi et al., 2008). The resulting NNW–SSE to NW–SE extension led to the formation of the Gulf of Lion passive margin and subsequent opening of the Ligurian back-arc basin (Hippolyte et al., 1993; Séranne, 1999; Séranne et al., 2021; Hemelsdaël et al., 2021; Bestani et al., 2016), temporarily overprinting WER-related extension during the Chattian. Thermochronological data and modeled thermal histories from the Tanneron and Maures massifs indicate heating between ~40 and 35 Ma and ~20–15 Ma (Boschetti et al., 2025). This heating was attributed to elevated geothermal gradients associated with Oligocene arc/back-arc magmatism and related intrusions cross-cutting the Maures–Tanneron basement, and/or to the Gulf of Lion crustal thinning and subsequent opening of the Ligurian basin (e.g., Séranne, 1999; Jolivet et al., 2020). Older AFT ages of 37–17 Ma from the Maures Massif (Morillon, 1997; Jakni, 2000) likewise likely record its thermal evolution during formation of the Gulf of Lion margin and opening of the Ligurian basin.

African–Eurasian convergence persisted through the Neogene, producing Alpine compression. In Provence, Alpine deformation probably began during the Langhian (Villeger, 1984; Blès and Gros, 1991), reached a paroxysm during the Tortonian (Clauzon et al., 2011), and continued into the Pliocene (Molliex et al., 2011). The Alpine compressional stress was mainly oriented NW–SE to NNE–SSW (Combes, 1984; Bergerat, 1987; Gaviglio and Gonzales, 1987; Baroux, 2000; Baroux et al., 2001; Delacou et al., 2004; Guignard et al., 2005; Cushing et al., 2008; Balansa et al., 2022). This event reactivated major E–W-trending folds inherited from the Pyrenean–Provençal contractional phase, including the Lubéron, Alpilles, Trevaresse and Ventoux structures (Tempier, 1987; Champion et al., 2000; Clauzon et al., 2011; Molliex et al., 2011; Lamarche et al., 2012; Lavenu et al., 2013; Guyonnet-Benaize et al., 2015), even though Alpine shortening in Provence remained overall limited (Bestani et al., 2016).

2.3. Timing of (meso)structure development

The sequence of (meso)structure development in the Mirabeau and Bimont anticlines, the Rians syncline and the Nerthe massif (Fig. 1) was

recently established by Zeboudj et al. (2025a,b) on the basis of field observations and paleostress reconstructions from fault-slip and calcite-twin data. Relative chronology, based on cross-cutting relationships among faults, veins and stylolites and on their attitudes relative to bedding, allowed us to distinguish structures related to the Pyrenean shortening from those that pre- or postdated it. Pyrenean structures developed under a compressional to strike-slip stress regime, with a N–S to NNE-SSW-oriented σ_1. Many formed during layer-parallel shortening (LPS), while the strata were still horizontal, and consist, after unfolding, of bed-perpendicular N–S to NE-SW veins and E–W tectonic stylolites, N–S dextral and NE–SW sinistral strike-slip faults, and E–W to WNW–ESE reverse faults. Structures formed during fold growth mainly include flexural-slip surfaces, E–W to WNW–ESE reverse faults with variable dips as a result of their development during progressive limb tilting, and ~E–W veins parallel to fold axes that developed in response to strata curvature at fold hinge. Major ~ E–W-striking thrust zones are also associated with this main contractional stage. Mesoscale faults formed during late-stage fold tightening (LSFT), i.e., in response to continuing shortening while the fold has locked and strata tilting was over (Tavani et al., 2015; Lacombe et al., 2021) have broadly similar orientations to LPS-related faults but crosscut tilted strata irrespective of bedding dip (Fig. 2). Apart from burial-related BPS, pre-Pyrenean structures consist mainly of sets of bed-perpendicular fractures with variable orientations (NW–SE, E–W, and NE–SW after unfolding) that are unrelated to the Pyrenean compressional stress field. Calcite-twin based paleostress reconstructions instead support their formation under a pre-Pyrenean extensional regime, with a roughly NNE-SSW oriented σ_3 (Fig. 2). Similar pre-Pyrenean and Pyrenean fault–vein–stylolite associations were observed throughout the investigated structures, although their orientations and internal sequences may vary slightly. Post-Pyrenean structures cut across Pyrenean folds and thrusts and mainly consist of N-S and E-W striking subvertical veins and normal faults (Fig. 2).

As part of ongoing efforts to date brittle deformation in FTBs (see review by Lacombe and Beaudoin, 2024), the timing of the major thrusts and mesoscale fault and vein populations in Provence was further constrained by U–Pb dating of syn-kinematic calcite mineralizations. The U-Pb ages refined the previously established sequence of (meso)structure development by robustly assigning faults and veins to the successive regional contractional and extensional tectonic events (Fig. 2): the Albian–Cenomanian Durancian uplift and associated NNE–SSW extension (110–90 Ma), ~N–S Pyrenean contraction (81–35 Ma), E–W Oligocene extension (35–25 Ma) and NNW–SSE Oligo-Miocene extension (30–18 Ma), related to WER and LPR, respectively. The NW–SE to NNE–SSW Alpine shortening likely started at ~15 Ma but no U-Pb ages are available. U-Pb ages further revealed polyphase vein sets with similar strikes that were reactivated or progressively densified during successive tectonic events (Zeboudj et al., 2025b). These include N–S vertical veins formed during the Pyrenean shortening and the Oligocene extension, and E–W vertical veins formed during the NNE–SSW Albian–Cenomanian extension, the N–S Pyrenean shortening, and the NNW–SSE Oligo-Miocene extension. Finally, the U-Pb ages support the idea that Pyrenean shortening in Provence (1) occurred in two main phases, 81–69 Ma and 59–34 Ma, coeval with the inversion of the pre-Pyrenean rift and the main Pyrenean collision, respectively, separated by a period of tectonic quiescence, and (2) propagated in sequence

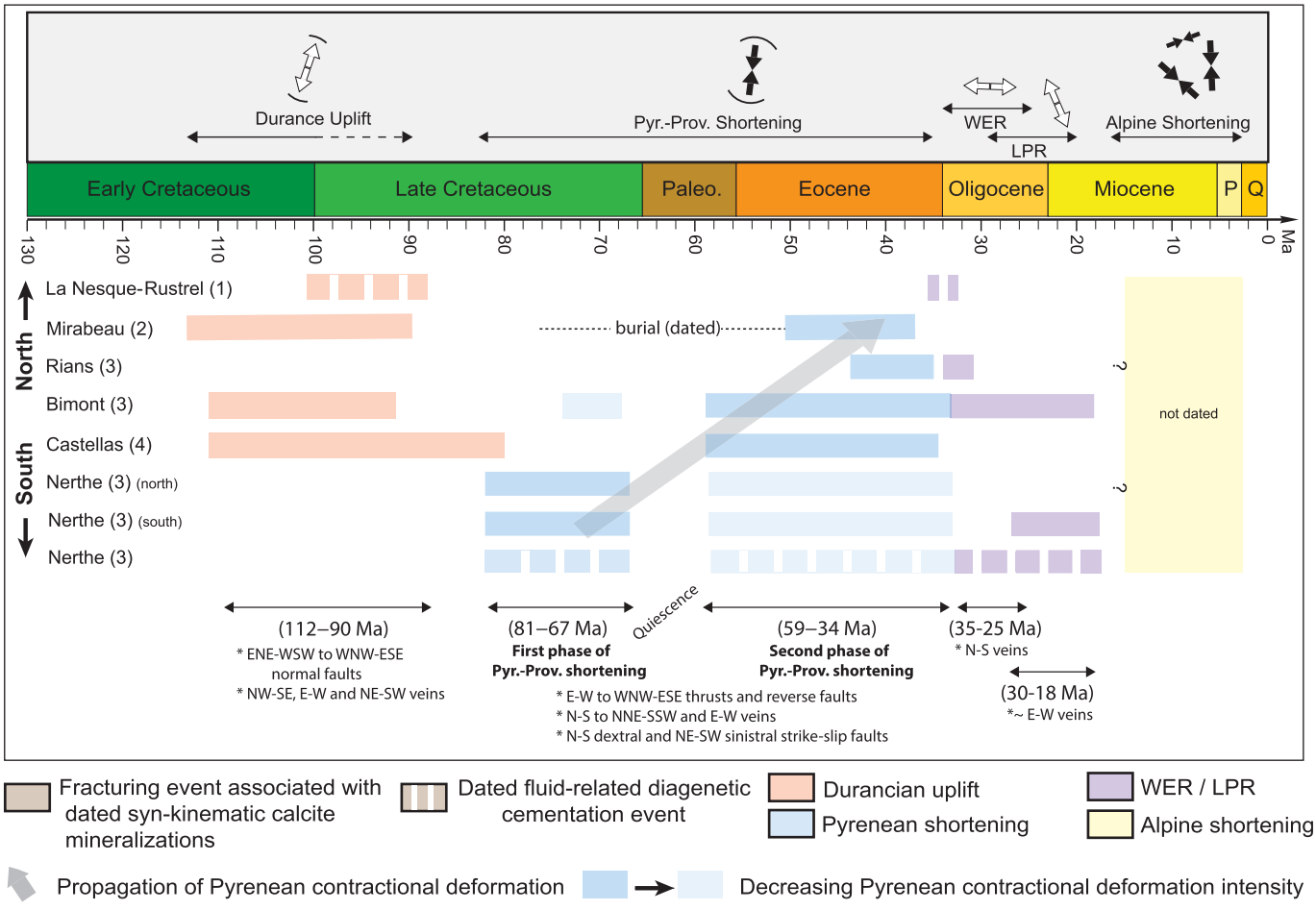


Fig. 2. Chart reporting the tectonic history of Provence since the early Cretaceous based on U-Pb geochronology. Data from (1): Godeau et al. (2018); (2) Zeboudj et al. (2025a); (3) Zeboudj et al. (2025b); (4) Corrêa et al., 2022.

northward, i.e., forelandward (Zeboudj et al., 2025b, Fig. 2).

2.4. The studied structures

2.4.1. The Mirabeau anticline

The Mirabeau fold is a major contractional structure associated with the AMDF system (Zeboudj et al., 2025a, Fig. 1). It is a WNW–ESE-trending, NE-verging fault-propagation anticline (Guyonnet-Benaize et al., 2015), characterized by a subvertical northern forelimb and a southern backlimb dipping ~40° to the south. The fold exposes predominantly Mesozoic carbonate strata, beginning with a ~90 m-thick Lower Triassic succession overlain by ~1 km of Jurassic to Valanginian–Hauterivian limestones with minor marl interbeds. The Barremian (Urgonian) platform limestones, the overlying ~300 m-thick Aptian–Albian limestone and marl succession, and the entire Late Cretaceous and Paleocene–Eocene–Oligocene successions are absent. The Mesozoic strata are unconformably overlain by gently dipping Miocene (Serravallian–Tortonian) shallow-marine deposits.

The outcropping strata show widespread pressure-solution features (sedimentary BPS and tectonic stylolites), veins and faults (mainly reverse and strike-slip faults, some appearing as normal faults as a result of strata tilting) (e.g., Kaci, 2019; Lamarche et al., 2020). Most of these structures were dated between 50 and 37 Ma and are related to the Pyrenean shortening (Zeboudj et al., 2025a) (Fig. 2). Few extensional NW-SE and NE-SW striking veins and a WNW-ESE striking mesoscale normal fault dated between 112 and 90 Ma were related to the Durancian uplift and related NNE-SSW extension (Zeboudj et al., 2025a).

Because the Mirabeau anticline lies close to the axis of the Durancian high, Cretaceous erosion was particularly intense. The removal of ~700 m of the initial ~1 km-thick Early Cretaceous succession, local truncation of Late Jurassic strata and bauxite development indicate that ~700–1000 m of Mesozoic formations were eroded during the Late Cretaceous (Molliex, 2009; Guyonnet-Benaize et al., 2010). A further ~500 m of denudation likely occurred during the Pyrenean shortening, removing the Late Cretaceous–Paleocene–Eocene syntectonic cover and exposing the Jurassic core of the fold. Bruna et al. (2013) estimated ~850 m of erosion and uplift related to the Pyrenean orogeny north of the nearby Vautubière anticline. Where preserved, Oligocene formations onlap the pre-existing folded structure, indicating that the anticline remained a topographic high at that time. The Mirabeau fold was therefore probably only partially covered and not deeply buried during the Oligocene relative to the adjacent basins, with burial likely less than 500 m (~200 m according to Bruna et al., 2013, north of the Vautubière anticline).

2.4.2. The Rians syncline

The Rians Basin (Fig. 1) is a NW-SE-trending syncline bounded to the NE by the Vautubière anticline, in the west by the Concors thrust, and in the south by the Sambuc anticline (Espurt et al., 2012). The sedimentary series comprises ~1500 m of marine limestones and marls of the Triassic and Jurassic, overlain by ~400m thick massive Berriasian and Valanginian marine limestones and shales exposed in the northern part of the basin. The foreland sequences start by mid Campanian breccia and late Campanian siltstones and sandstones covered by the Maastrichtian lacustrine limestones and fluvial siltstones. The Cenozoic formations consist of Paleocene breccia, lacustrine limestones and siltstones.

No major structure was observed in the weakly deformed Rians basin, but Zeboudj et al. (2025b) reported N-S and ENE-WSW subvertical veins that yielded U-Pb ages between 36 and 33 Ma, suggesting their opening during the late Pyrenean shortening and the subsequent Oligocene extension. A jog associated with a sedimentary BPS in sub-horizontal strata yielded a U-Pb age of ~45 Ma, supporting the idea that the Rians Basin was still experiencing burial until the middle Eocene and that the Pyrenean shortening likely occurred between ~45 and 36 Ma there (Fig. 2) and weakly affected the internal part of the basin.

While the late Cretaceous strata of the Rians syncline were presumably neither significantly buried (~200m of Paleocene-Eocene formations) nor uplifted during the Pyrenean shortening, the hiatus between the late Campanian and the Valanginian limestones and the occurrence of bauxites indicates a significant erosion during the Durancian uplift.

2.4.3. The Bimont anticline

The Bimont Lake area is located within the western segment of the Sainte-Victoire system and is structured by two ENE-to E–W-striking, N-dipping thrusts, known as the Bimont and the Reynauds thrusts (Espurt et al., 2012) (Fig. 1). The Bimont fold is a E-W trending, south verging anticline with a subvertical to slightly overturned southern limb.

Above 50 m of Rhaetian shales, the sedimentary succession there consist of roughly 1500–2000 m thick Jurassic limestones (with sometimes breccias and marls), overlain by a ~200-300m thick Berriasian-Valanginian strata. In the southern part of the fold, Campanian, Maastrichtian and Danian breccia formations unconformably overlie the subvertical late Jurassic strata. These breccia belong to preserved growth strata why testify the progressive development of the Bimont fold between the Campanian and the Paleocene. The folded series are unconformably overlain and sealed by Miocene deposits.

Like in Mirabeau, the outcropping strata exhibit abundant pressure-solution features (sedimentary BPS and tectonic stylolites), veins and faults (mainly reverse and strike-slip faults, some appearing as normal faults as a result of later tilting), most related to N-S to NNE-SSW Pyrenean shortening. Thrusting and fracture development seemingly occurred mainly in two stages, as indicated by U-Pb ages of syn-kinematic calcite mineralizations (Zeboudj et al., 2025b): 74-68 Ma and mainly 59-47 Ma (until 33 Ma), with the formation of the Bimont fold being likely achieved by ~57-55 Ma. While N-S veins primarily formed during the Pyrenean shortening, U-Pb dating revealed that some also formed during the Oligocene E-W extension. No fractures related to the Durancian uplift could be dated, but two calcite jogs along extensional tectonic BPS were dated between 110 and 96 Ma (Fig. 2).

During the Durancian uplift, the future Bimont fold underwent massive erosion. Bauxites developed in the eastern Sainte-Victoire and the Rians syncline and were covered by foreland latest Santonian-Campanian formations, suggesting the erosion of the late Hauterivian to Albian (?) strata, hence ~500m. During the Pyrenean shortening, syntectonic erosion, with deposition of the middle-late Campanian, Maastrichtian and Paleocene breccias directly onto late Jurassic limestones, possibly amounted up to 500 m.

2.4.4. The Nerthe massif

The Nerthe massif is an E–W-trending, tectonically complex structure bounded by the Mediterranean Sea, the Étang de Berre, and the Marseille Basin (Fig. 1). It is divided into tectonic blocks by major faults that developed during successive contractional and extensional events. The northern sector consists of a north-dipping monocline of Early Cretaceous limestones and marls forming part of the Istres syncline. The central sector comprises fault-bounded basins, including the Saint-Julien extensional basin, filled with Oligocene–Burdigalian lacustrine and continental deposits. The southern sector is characterized by northward thrusting, with Urgonian limestones emplaced over younger Aptian and Late Cretaceous units, forming a major thrust system rooted in the Triassic evaporites. At depth, the basement is cut by a south-dipping thrust (Bestani et al., 2016). Most contractional deformation, involving both thin- and thick-skinned structural styles, occurred during Pyrenean shortening. Two major E–W-trending anticlines associated with north- and south-verging thrusts, including the La Folie–Valapaux fault, were subsequently cross-cut by E–W-striking Oligocene normal faults. Early Burdigalian to Tortonian marine formations unconformably overlie the deformed structures, indicating that most tectonic deformation predates their deposition, although the Burdigalian strata were themselves affected by E–W-striking normal faults.

Veins, mesoscale faults and major thrusts were investigated for U-Pb

dating (Zeboudj et al., 2025b). In contrast to the main fault zones, the vein system is very complex, displaying veins with different orientations that yield similar U-Pb ages and veins with similar orientations that yield highly contrasted U-Pb ages. However, whatever their spatial scale, most structures could be interpreted as related to alternating strike–slip or compressional stress regimes with σ_1 roughly oriented N-S to NNE-SSW, and developed in two time periods, during the late Cretaceous (~81–67 Ma) and during the Eocene (~59–34 Ma). Zeboudj et al. (2025b) proposed that the main Pyrenean shortening in the Nerthe massif occurred during the latest Cretaceous, causing exhumation of folded strata and favoring downward fluid flow. Indeed, the authors reported clear markers of subaerial environments (dated as early as ~72 Ma and lasting until the Miocene, ~9.5 Ma), indicating that the range was close to emersion as soon as its structure started to develop. The second period likely corresponds to a late, minor component of renewed Pyrenean contraction and reactivation of earlier structures. Zeboudj et al. (2025b) also reported U-Pb ages between ~110 Ma and ~93 Ma for variously oriented veins that are likely related to the Durancian uplift and associated NNE-SSW extension. Finally, an E-W vein yielded a 20 Ma U-Pb age, consistent with the Oligo-Miocene NNW-SSE extension that created the Valtrède and the Laurons–Ensuès normal faults bounding the Saint Julien extensional basin.

In contrast to the northernmore folds, the Urgonian limestones are preserved in the Nerthe massif, which indicates that erosion during the Durancian uplift remained moderate (~200–400 m). Erosion occurred mainly during the Pyrenean-Provencal compression, estimated to 800 to 1000 m as suggested by structural cross sections (Tempier, 1987). Much of the material removed from the crest of the Nerthe massif ended up in the Oligocene Estaque conglomerate, which contains reworked Urgonian limestone pebbles from the Nerthe.

3. Material and methods

3.1. Sampling strategy and material

Unlike major faults, sub-seismic fractures like veins are common and readily accessible features in sedimentary strata, with their mineralizations recording fluid migration during successive stages of deformation. However, the isotopic signatures of veins are often more scattered than those of fault zones, owing to local chemical variability and uncertainties in assigning the veins to specific sets based solely on their orientation (Beaudoin et al., 2011, 2013, 2014; Berio et al., 2022). Extensive U–Pb dating of syn-kinematic calcite helps overcome this uncertainty by enabling robust assignment of mesoscale faults and vein sets to successive deformation stages (Zeboudj et al., 2025b). At Mirabeau and Rians, where major thrusts are not exposed, we sampled pervasive mesostructures such as veins, mesoscale faults and stylolites (Fig. 3A–E). Conversely, at Bimont and La Nerthe, we sampled syn-kinematic calcite from mesostructures as well as from the damage zones and fault cores of exposed thrust zones (Fig. 3F, G–I). Host rocks were also sampled. The locations of sampling sites in the investigated structures and the type of analyses performed on samples from each site can be found in the Supplementary Material S1 and S2, respectively.

For all the calcite samples, the petrographic analyses carried out on polished thin-sections using an optical microscope Zeiss AxioSkop 40 (Carl Zeiss Light Microscopy, Göttingen, Germany) equipped with a Nikon D5100 SLR camera (Nikon Corporation, Tokyo, Japan, and X-ray diffraction (XRD) (Bruker D2 Phaser diffractometer with X-Ray wavelength of 1.54056 Å) confirmed the calcite nature of the vein filling, fault coating and rock matrix (Zeboudj et al. 2025a, 2025b). The diagenetic state of the calcite mineralization (e.g., the absence of later alteration) was further investigated using cathodoluminescence OPEA (Laboratoire Optique Électronique Appliquée, Paris, France) Cathodine equipped with a cold cathode. The latter were performed with replicable parameters, 50–60 mTorr vacuum, 15 kV voltage, and 200 μA electron beam. All these analyses were conducted at ISTeP (Institut des Sciences de la Terre de Paris), Sorbonne Université, Paris, France.

BPS with peaks perpendicular to the dissolution plane (Fig. 3A and B) were sampled by hand or though coring in late Jurassic strata (Tithonian) at Mirabeau, early Cretaceous (Barremian) strata in the Nerthe Massif and late Cretaceous (Maastrichtian) in Rians.

3.2. Oxygen and Carbon stable isotopes

For O-C isotope measurements, 30 to 50 μg of powder were sampled from the syn-kinematic calcite mineralizations and the surrounding host-rocks, using a computer-assisted micromill drill to avoid any contamination between mineralization and host rocks. The powder was placed in glass vials and reacted with anhydrous orthophosphoric acid at 70°C to extract CO_2 gas, itself ionized in the spectrometer. The isotope ratios of oxygen ($^{18}O/^{16}O$) and carbon ($^{13}C/^{12}C$) were obtained by Isotope-Ratio Mass Spectrometry (IRMS). The spectrometric equipment couples an automatic sample preparation device (KIEL IV Carbonate) and an analysis section (DELTA V Advantage) from Thermo Fisher Scientific at ISTeP.The measured isotopic ratio reported in permil relative to the Vienna Pee Dee Belemnite (‰VPDB) are with an accuracy of 0.03‰ and 0.08‰ for carbon and oxygen, respectively.

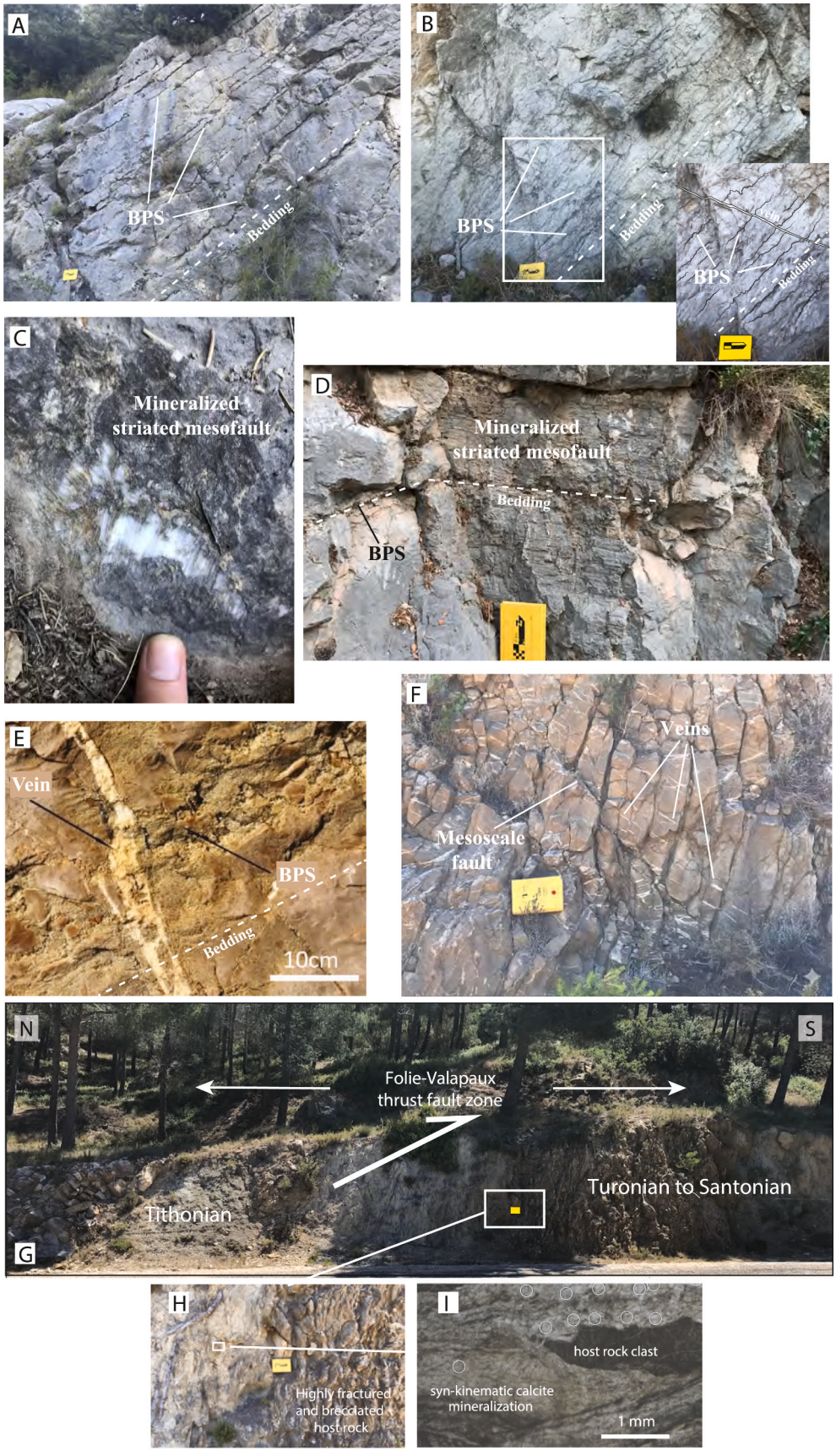
3.3. Clumped-isotope thermometry (Δ_{47})

Clumped isotope analyses were performed at the Δ_{47} facility of the Laboratoire des Sciences du Climat et de l'Environnement (LSCE, Gif-sur-Yvette, France). Powdered samples from calcite mineralizations were analyzed three times each, following a protocol consisting of converting 3.5 to 4 mg of $CaCO_3$ to CO_2 by reaction with phosphoric acid at 90°C in a stirred common acid bath for 15 min. After cryogenic removal of water, CO_2 was passed through a purification column (1 m long, 2.1 mm internal diameter) filled with Porapak Q (50/80 mesh) in a flow of Helium at 25 mL/min, then transferred to an Isoprime 100 dual-inlet mass spectrometer equipped with 6 F collectors (m/z 44–49), with high-gain amplification (10^{12} Ω) applied to the m/z 47 cup.

Background-corrected ion current ratios (δ45 to δ49) were converted to $\delta^{13}C$, $\delta^{18}O$, and 'raw' Δ_{47} values as described by Daëron et al. (2016), using the IUPAC oxygen-17 correction parameters. The ETH carbonate standards (Bernasconi et al., 2018) were used to compute the isotopic composition ($\delta^{13}C$, $\delta^{18}O$) of our working reference gas, assuming an oxygen-18 acid fractionation factor of 1.00813 (Kim et al., 2007). Raw Δ_{47} values were then converted to the I-CDES reference frame (Bernasconi et al., 2021) using a pooled regression approach (Daëron, 2021) as implemented by the D47crunch library (v.2.5.3). Full analytical errors are derived from the pooled external Δ_{47} reproducibility ($\sigma = 8.6$ ppm) of unknowns and standards (Nf = 154) and conservatively account for the uncertainties in raw Δ_{47} measurements as well as those associated with the conversion to the I-CDES reference frame (Daëron, 2021). Calcite formation T was estimated based on the composite OGLS23 calibration of Daëron and Vermeesch (2024). A complete analytical report is provided as Supplementary Material S3.

3.4. $^{87}Sr/^{86}Sr$ ratios

Strontium isotope analyses were performed by SEDISOR (Plouzané, France). Approximatively 0.5g of sample powder was digested in pre-cleaned Savillex® vial with 2 ml of ultrapure HNO_3 1M. Strontium was isolated from the sample matrix by ion-exchange chromatography using a Sr-Spec resin (Triskem®) following a procedure modified after Pin and Zalduegui (1997). Strontium was eluted with 2 ml of hot ultrapure H_2O. Samples are loaded on W filaments for thermal ion mass spectrometer (TIMS) measurements. Sr isotope ratios were measured in static mode on a Thermo Scientific TRITON mass spectrometer at the PSO (Pôle de Spectrométrie Océan), Brest, France. All measured ratios are normalized to $^{86}Sr/^{88}Sr = 0.1194$ and the Sr isotope compositions of standard solution NBS987 is routinely measured with a frequency of 5



(caption on next page)

Fig. 3. Field examples of structures sampled and investigated in our geochemical-tectonic study. A-B: Examples of tilted burial-related BPS (Bedding-Parallel Stylolites) in the Mirabeau anticline as used for roughness analysis. C-D: Examples of mineralized mesoscale striated faults (C: Mirabeau anticline; D: Rians syncline). E-F: Examples of mineralized veins (E: Mirabeau anticline; F: La Nerthe massif). G: Example of sampled thrust fault zone in the Nerthe massif, with zooms of the fractured, brecciated and mineralized internal structure of the fault zone (H,I). White circles correspond to laser ablation spots for U-Pb dating (Zeboudj et al., 2025b).

analyses every two samples. During the analytical session, NBS987 gave a $^{87}Sr/^{86}Sr$ ratio of 0.710238±0.000005 (2σ, n = 4).

3.5. Rock Eval pyrolysis of the organic matter

The organic matter content and maturity of host rocks was analyzed using a Rock-Eval 6 Turbo instrument (ISTeP, Sorbonne Université) in Bulk Rock/Basic mode, as described by Behar et al. (2001). Pyrolysis of the rock at temperatures between 300°C and 400°C enables the determination of the S2 parameter, which corresponds to the quantity of hydrocarbons (in mg per g of rock) released by the organic matter (kerogen). When extrapolated to geological conditions, S2 represents the amount of hydrocarbons the source rock would generate if heated to a sufficient temperature and duration for the organic matter to crack. In petroleum exploration, this parameter is termed the petroleum potential (Espitalié et al., 1977). The S2 analysis yields T_{max} (°C), the temperature at which the maximum amount of hydrocarbons is released. T_{max} is interpreted in terms of the thermal maturity of the organic matter, enabling the practical identification of oil- and gas-generating zones (Espitalié and Burrus, 1986; see also Supplementary Material S4).

3.6. BPS roughness inversion for stress

Stylolite roughness inversion is a recent paleopiezometric technique using stylolite roughness—the height difference between points along a profile at a given horizontal scale—to record stress magnitudes when pressure-solution ceased (Beaudoin and Lacombe, 2018). Local dissolution gradients favor growth and create roughness, while opposing forces smooth the surface: small-scale surface energy (controlled by dissolving material chemistry) and large-scale (>1 mm) elastic energy (Hooke's law), governed by material mechanical properties like Poisson ratio (ν) and Young modulus (E). Treated as a signal, stylolite roughness exhibits two power laws on a log–log plot, each characterized by a Hurst roughness exponent (Schmittbuhl et al., 2004), with values of 1.1 and 0.5 for the power law related to surface energy and to elastic energy, respectively (e.g., Toussaint et al., 2018). The observation scale at which the controlling forces switch from surface energy-dominated to elastic energy-dominated, called crossover length (L_c), is defined as: $L_C = \gamma E/\beta\sigma_m\sigma_d$, where L_c is the crossover length (in mm), E the Young modulus of the rock (in Pa), γ the solid–fluid interfacial energy (in Jm^{-2}), β a dimensionless constant depending on the Poisson ratio (ν) [$\beta = \nu(1-2\nu)/\pi$], σ_m is the mean stress magnitude [$(\sigma_1+\sigma_2+\sigma_3)/3$] and σ_d the differential stress magnitude ($\sigma_1-\sigma_3$).

In the case of BPS developed in response to burial-related compaction under a vertical maximum principal stress, it is assumed that $\sigma_V \gg \sigma_H = \sigma_h$ (uniaxial strain hypothesis), so the expression of σ_v can be simplified as $\sigma_v^2 = \gamma E/\alpha L_c$ (eq. (1)), with α being a constant defined as $= (1-2\nu)(1+\nu)^2/30\pi(1-\nu)^2$. The value of L_c can be determined by the analysis of the stylolite roughness as a 2D signal using either the Fourier Transform (Fourier Power Spectrum, FPS) or the Average Wavelet Coefficient (Daubechies D4 wavelets, AWC). BPS samples were cut perpendicular to the plane of the stylolite, each cut was polished and scanned and each scan was digitized either manually on pixel-based drawing software or automatically with color and shape-based segmentation. The signal analysis was conducted on an 8-bit high-resolution image (12,800 dpi) of the 1D stylolite track over a length ranging from a few cm to 5 cm using Python scripts adapted from previously published Matlab scripts (Ebner et al., 2009; Labeur et al., 2024). For each log–log plot, a non-linear regression with slopes set according to the expected Hurst coefficients was fitted through the binned data. The L_c value is defined by the change in slope of the regression lines, with an uncertainty of 23% (Rolland et al., 2014). In this study, L_c was given using AWC signal analysis using Daubechies D4 wavelets (Simonsen et al., 1998; Ebner et al., 2009), and the resulting σ_v was converted into depth (z) using $\sigma_v = \rho gz$, where g is the gravitational acceleration (9.81 ms^{-2}) and ρ is the mean density of the overlying sedimentary column. The magnitude of the vertical principal stress σ_v and therefore the estimated depth are determined with 12% uncertainty, regardless of the past geothermal gradient and fluid pressure (Beaudoin and Lacombe, 2018). The Stylolite Roughness Inversion Technique (SRIT hereafter) has been extensively evaluated in terms of its underlying assumptions and limitations (Koehn et al., 2007, 2012; Ebner et al., 2009; Toussaint et al., 2018; Beaudoin et al., 2019), and has been successfully applied across a range of sedimentary basins and FTBs (Ebner et al., 2009; Rolland et al., 2014; Bertotti et al., 2017; Beaudoin et al., 2016, 2019; Lacombe et al., 2021; Labeur et al., 2021, 2024; Zeboudj et al., 2023). More recently, the reliability of SRIT as a depth gauge has been independently supported by the combined application of BPS roughness inversion and clumped-isotope thermometry (Beaudoin et al., 2025).

In order to calculate L_c, the static Young modulus (E) must be estimated, as the most variable elastic parameter of carbonate rocks (Regnet et al., 2019). We use a non-destructive Schmidt hammer (Silver Schmidt OS8200 type N, manufactured by PROCEEQ), measuring the rebound of a spring-loaded piston pressed orthogonally against the rock surface. The rebound value R proxies surface stiffness, enabling E calculation via Aydin and Basu's (2005) empirical relationship: $E = 0.72\ e^{(0.05\,R)}$ (eq. (2)). Although this relationship was derived from laboratory tests on granite and the influence of lithology on rebound values remains insufficiently constrained, it provides the best available approximation of the static Young's modulus when using a Type N Schmidt hammer. At each site, 20 to 50 orthogonal rebound measurements were averaged to obtain a single representative value. To minimize the influence of local heterogeneities and remove potential outliers, a moving incremental average was calculated until the mean rebound value stabilized (Supplementary Material S5). The E values derived from Schmidt hammer measurements are representative of the present-day mechanical behavior of the rocks. Whether these values adequately represent the elastic moduli at the time of deformation, particularly under burial conditions, has been a recurring issue (Bauer et al., 2017; Lamarche et al., 2012; Petrie et al., 2012). However, mechanical tests have shown that the static Young's modulus increases with burial depth until reaching a plateau, and that subsequent exhumation does not significantly affect this plateau value (English, 2012). We therefore consider the use of Schmidt hammer measurements to be a valid approach for SRIT, provided that the associated uncertainty is properly accounted for.

4. Proposed new integrative workflow

In this contribution, we propose a new workflow that integrates structural, geochemical and geochronological datasets to reconstruct (1) the evolution trend of the fluid system and (2) the depth–T–d–t trajectories of host carbonate reservoir rocks during the Cretaceous–Tertiary times (Fig. 4).

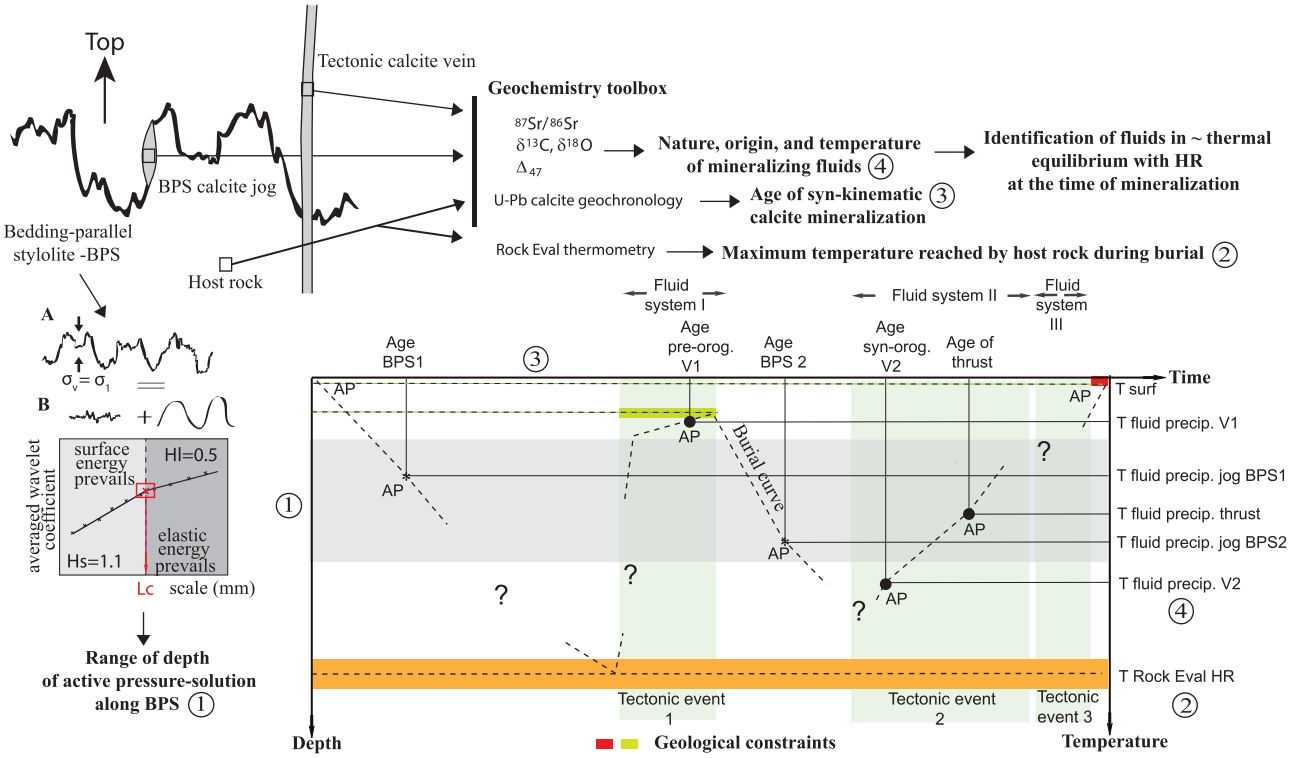


Fig. 4. Workflow of the proposed structural-geochemical-paleopiezometric-geochronological multi-proxy study of mineralized structures and their host rocks that enables reconstruction of a burial-time model with set anchor points (AP).

First, we use $\delta^{18}O$, $\delta^{13}C$, Δ_{47} and $^{87}Sr/^{86}Sr$ ratios measured in syn-kinematic calcite to constrain the origin of past fluids, calcite precipitation temperatures and the extent of fluid–rock interactions (Evans and Fischer, 2012; Beaudoin et al., 2014, 2015, 2022) during successive deformation events. This approach highlights the main trends in fluid evolution, such as the remobilization of formation fluids or the ingress of meteoric fluids, and identifies periods or tectonic events characterized by distinct mineralizing fluids.

Second, to constrain the late Jurassic, Early Cretaceous and Late Cretaceous carbonate depth–T–d–t trajectories, we use BPS populations as indicators of active pressure-solution depth ranges (Fig. 4). Because BPS roughness can fossilize prematurely while strata continue to be buried, and because sampling is necessarily limited, BPS paleopiezometry conservatively provides a minimum estimate of burial depth (Fig. 4). When BPS are associated with dated calcite-filled jogs, the active pressure-solution depth can be dated, providing a depth–t anchor point (Fig. 4). These depth estimates remain entirely independent of assumptions about the past geothermal gradients.

Temperature constraints on the depth–T–d–t trajectories are derived primarily from organic-matter pyrolysis that constrains maximum burial temperatures of host rocks (Fig. 4), supplemented by calcite isotope analyses. Following fluid characterization for each tectonic event, we assess whether the mineralizing fluids were at thermal equilibrium with the host rocks during calcite precipitation, thereby allowing precipitation temperatures to be used as proxies for host-rock temperature (Fig. 4). This requires either (1) calcite precipitation from a local fluid without significant advective heat transport or (2) the identification of downward-migrating fluids (e.g., meteoric fluids infiltrating from the surface or downward marine fluid flows), such that precipitation temperatures are at or below the geothermal temperature expected at depth. To ensure that the calcite is at thermal equilibrium in the latter case, we assume that a fluid geochemically buffered by the host rock reflects a low fluid/rock ratio, which likely minimizes local thermal perturbations. Consequently, the fluid is also expected to be thermally buffered by the host rock. Converting temperature to depth requires assumptions about the geothermal gradient, which must be tested against independent depth constraints. Such indirect temperature constraints are particularly valuable when U–Pb ages are available for the mineralization, as they provide T–d–t anchor points when fractures have been dated and confidently assigned to a specific deformation event (Fig. 4).

Remarkably, some BPS that provide depth constraints also contain jogs with dated calcite infills for which precipitation temperatures have been determined. Jog calcite precipitated from fluids at thermal equilibrium with the host rocks because pressure-solution development and the small size of the jogs limited large-scale fluid migration, whereas local pressure drops associated with crack development pumped fluids into the jogs and triggered calcite precipitation (Beaudoin et al., 2025). Here, the combination of roughness analysis, U–Pb geochronology, and clumped isotope thermometry provides a first-order depth–T–t anchor point for reconstructing host-rock burial history (Fig. 4). This constraint remains independent of the past geothermal gradient while also helping to constrain that gradient for a given surface temperature.

Finally, these geochemical depth–T–d–t constraints are integrated with geological constraints, including subaerial exposure of late Jurassic–Early Cretaceous rocks and bauxitization during the Durancian uplift; syn-tectonic erosion and deposition of Late Cretaceous–Paleocene breccia during the Pyrenean shortening; and Miocene deposits unconformably overlying folded Jurassic–Cretaceous strata, to constrain the Late Jurassic–Cretaceous burial history of the reservoir rocks (Fig. 4).

5. Results

5.1. $\delta^{18}O$ and $\delta^{13}C$ signatures

The $\delta^{18}0$ and $\delta^{13}C$ values of the 166 analyzed calcite mineralizations collected from faults and veins range between −15.13‰ and −3.15‰ VPDB considering $\delta^{18}0$ and from −7.93‰ to +4.25‰ VPDB considering $\delta^{13}C$ (Fig. 5A). In host rocks, the $\delta^{18}0$ ranges from −12.05‰ to −2.06‰ VPDB and the $\delta^{13}C$ ranges from −7.44‰ to +2.36‰ VPDB (Fig. 5B). It is noteworthy that there is no significant difference in these values among

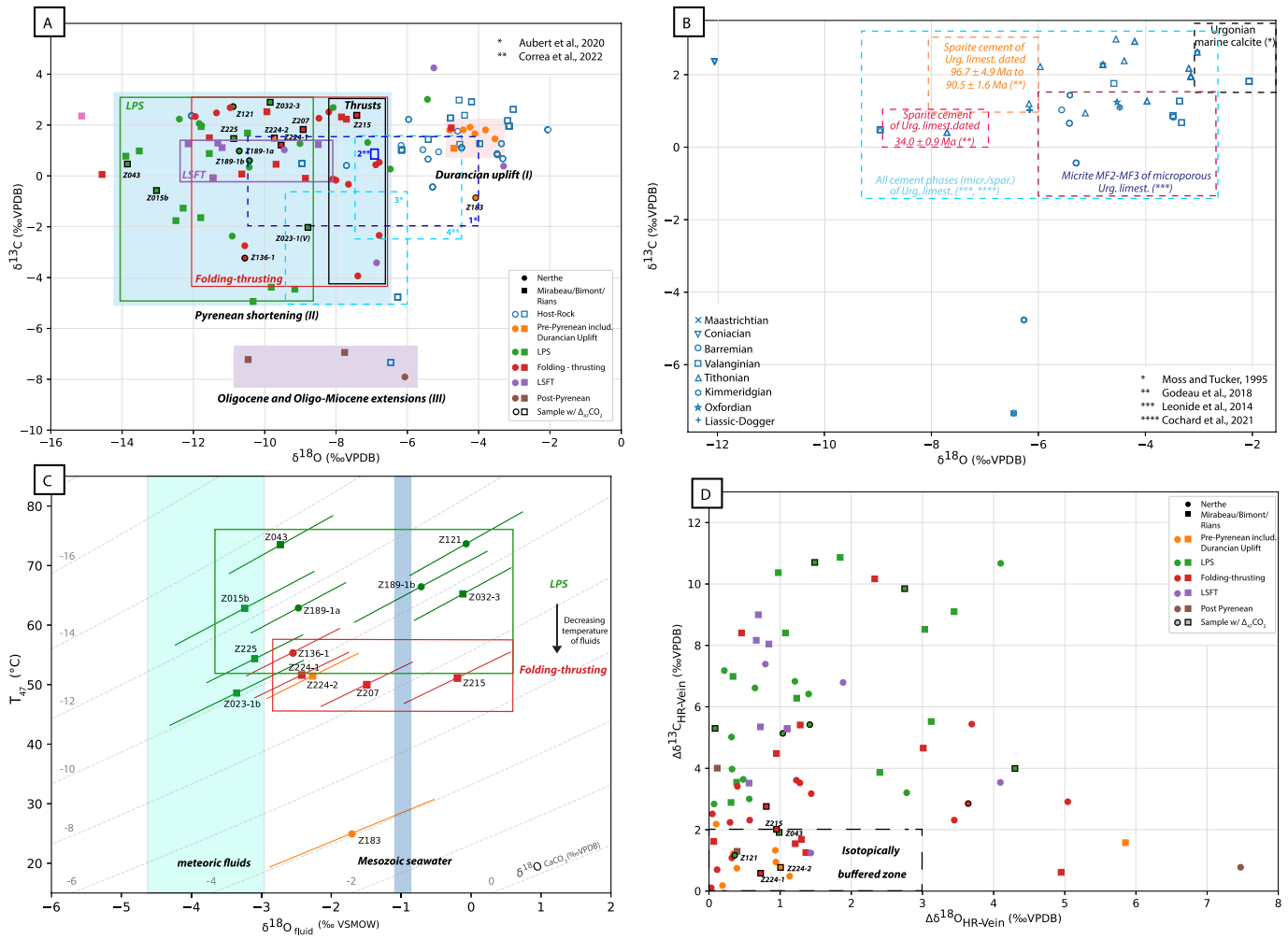


Fig. 5. A. Isotopic signatures $\delta^{13}C$ versus $\delta^{18}O$ of syn-kinematic calcite mineralization from veins and faults. Solid colored frames gather the isotopic values of samples belonging to the same structural event: LPS stands for Layer-Parallel Shortening, and LSFT for Late Stage Fold Tightening. Regional data from the literature are reported as dashed colored frames: 1*: Durancian syn-normal faulting mineralizations; 2**: Durancian syn- normal faulting mineralizations dated ~90 Ma; 3*: Pyrenean syn-strike-slip faulting mineralizations; 4**: Pyrenean syn-strike-slip faulting mineralizations dated ~50-40 Ma (after Aubert et al., 2020 and Corrêa et al., 2022). Labelled samples correspond to samples for which T_{47} is available (see Fig. 5C). B. Isotopic signatures $\delta^{13}C$ versus $\delta^{18}O$ of host rocks. Relevant data from the literature are reported as dashed frames (after Moss and Tucker, 1995; Godeau et al., 2018; Léonide et al., 2014; Cochard et al., 2021). C. T_{47} versus $\delta^{18}O$ fluid of syn-kinematic calcite mineralization from veins and faults. Same key as in A. D. Differences of isotopic signatures $\delta^{13}C$ between calcite mineralization and corresponding host rocks versus differences of isotopic signatures $\delta^{18}O$ between calcite mineralization and corresponding host rocks. The black dashed frame (2‰ by 3‰) represents the geochemical domain where syn-kinematic calcite samples can be considered as buffered with respect to their host-rock, see text for details.

the studied folds. However, the cross plot of O and C isotopic ratios of syn-kinematic calcite depicts 3 distinct clusters (Fig. 5A). The first type of vein-calcite isotopic signature is characterized by $\delta^{18}O$ values of −3‰ to −5‰ VPDB and $\delta^{13}C$ values of 0‰ to +2‰ VPDB (Domain I), overlapping with a large proportion of the host-rock isotopic compositions. The second domain (II) is defined by most of the data, in the range of −14‰ to −7‰ VPDB in $\delta^{18}O$ and of −2‰ to +3‰ VPDB $\delta^{13}C$. The third domain displays few signatures with $\delta^{18}0$ between −11‰ and −6‰ VPDB and $\delta^{13}C$ between −8‰ and −7‰ VPDB (domain III). Interestingly, Domain II encompasses most of the syn-kinematic calcite mineralization associated with structures formed during the Pyrenean shortening, whereas the other two domains correspond to veins attributed either to the pre-Pyrenean extensional event associated with the Durancian uplift (Domain I) or to the post-Pyrenean Oligocene–Miocene extensional events (Domain III) (Zeboudj et al., 2025a, 2025b). Within Domain II, two main trends can be identified. First, mineralization associated with early, layer-parallel shortening (LPS)-related mesostructures tends to be more depleted in ^{18}O, although with some overlap, than mineralization associated with mesostructures formed during LSFT and during the main shortening phase (folding and thrusting). Second, the mineralizations associated with mesostructures (veins and mesoscale striated faults) are overall more depleted in ^{18}O than those associated with the major thrust zones (Fig. 5A). Detailed results are provided in Supplementary Material S2.

5.2. Δ_{47} signatures

The values of Δ_{47} (‰ I-CDES) of the 15 analyzed calcite mineralizations range between 0.4767 and 0.5936. Based on the OGLS23 calibration of Daëron and Vermeesch (2024), these values correspond to calcite precipitation temperatures (T_{47}) ranging from 24.9 ± 5.7°C to 73.6 ± 5.3°C (95% CL, Fig. 5C). Although we did not perform any kinetic modeling, the expected alteration of the temperature by potential solid-state reordering (e.g., Hemingway and Henkes, 2021) is less than the analytical uncertainty, as the maximum temperature reached by the strata is below 100°C and as the strata likely remained below 80°C during most of their burial history. The $\delta^{18}O$ signatures of the parent fluids from which calcite precipitated were determined using the fractionation equation of Kim and O'neil (1997) in order to account for the out-of-equilibrium character of precipitation. They range between

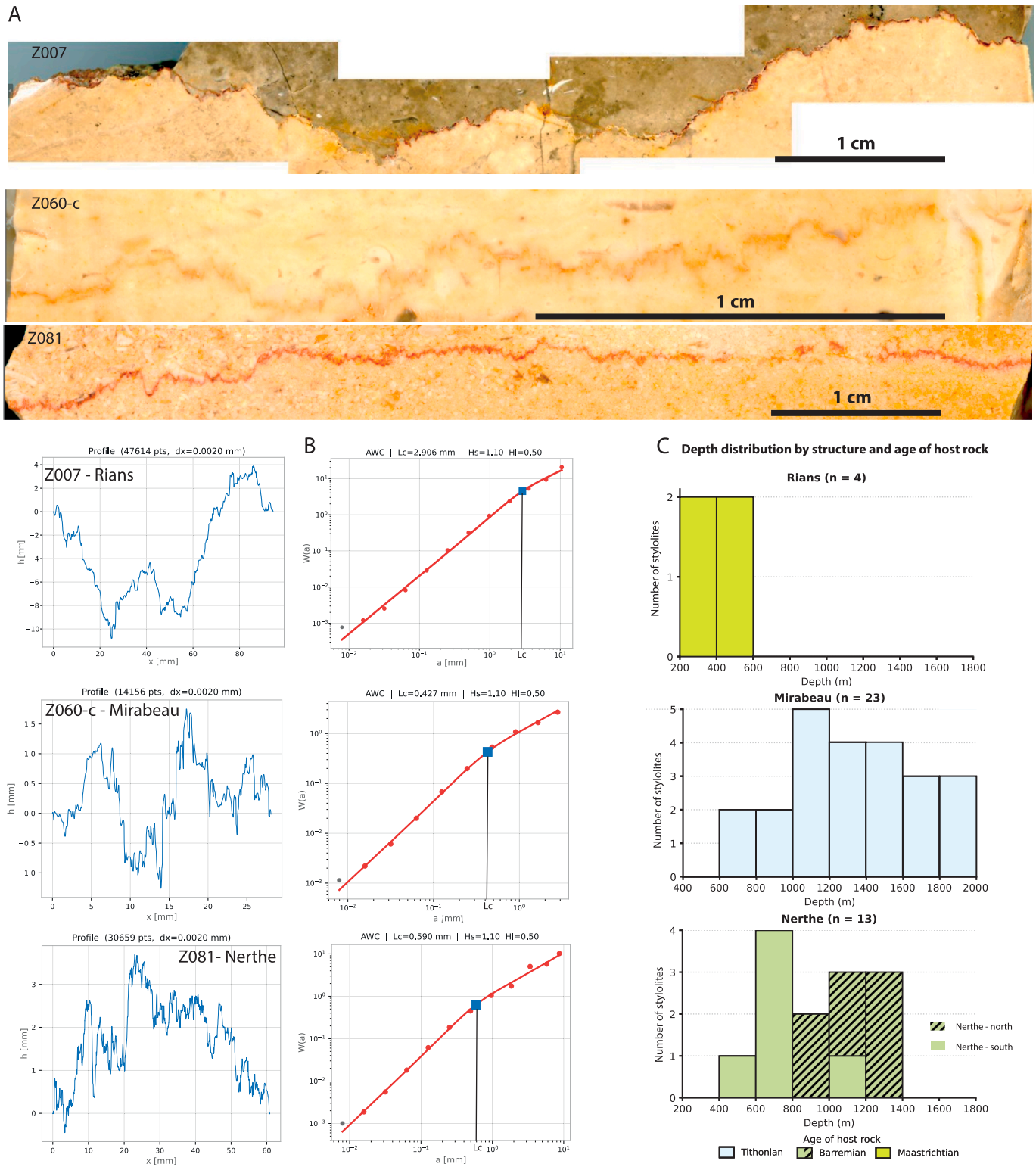


Fig. 6. A. Photographs of slabs of limestone rocks from the areas investigated showing BPS. Sample Z007 (Rians, Maastrichtian), Z060-c (Mirabeau, Tithonian) and Z081 (Nerthe, Barremian). B. Signal analysis of the BPS showed in A using AWC (left-hand side: the extracted track, right-hand side: the binned AWC signal with a dual-regression curve with set slopes). C: Depth distribution of the end of activity of pressure solution along BPS by structure and age of host rock. Note that the inversion shown in B illustrates each of the trends exhibited on C.

-3.6 ± 0.7‰ VSMOW and 0.2 ± 0.8‰ VSMOW (95% CL). With respect to the deformation event (Durancian uplift, Pyrenean LPS and Pyrenean folding and thrusting), differences arise, with pre-Pyrenean $\delta^{18}O_{fluid}$ values/precipitation temperatures ranging between -2.2 ± 0.7‰ and -1.7 ± 1.2 VSMOW/51.5 ± 3.9°C and 24.9 ± 5.7; LPS related values ranging between -3.3 ± 1.0 and 0.0 ± 0.8‰ VSMOW/48.6 ± 5.5 and 73.7 ± 5.4°C; and folding-thrusting -related values ranging between -2.5 ± 0.7 and 0.2 ± 0.8‰ VSMOW/55.5 ± 4.0°C and 51.1 ± 4.5. The detailed results are given in Supplementary Material S2 and S3.

5.3. $^{87}Sr/^{86}Sr$ signatures

The measured $^{87}Sr/^{86}Sr$ ratios of the 13 analyzed calcite mineralizations are low and rather homogeneous despite the range of ages of the host rocks and the variety of structures from which syn-kinematic calcites were sampled, between 0.70735 and 0.7080. The detailed results are given in Supplementary Material S2.

5.4. Maturity of host rock organic matter

The organic content of one sample collected from the Tithonian strata at Mirabeau is low (0.9 wt %) but was sufficient to produce a small amount of hydrocarbons during pyrolysis (S2 = 0.47 mg/g). There is no free hydrocarbon (S1 < 0.01 mg/g). The T_{max} value for the sample is 441.5 ± 2°C. The detailed results are given in Supplementary Material S2 and S4.

5.5. Inversion of stylolite roughness for stress

Among the 53 BPS sampled from host rocks spanning different stratigraphic ages in the three structures investigated, 40 BPS yielded exploitable inversion results (i.e., a well constrained L_c value) using SRIT: 4 in the Rians syncline (Maastrichtian), 23 in the Mirabeau anticline (Tithonian), and 13 in the Nerthe massif (Barremian). A minimum stylolite length of 2.1 cm was required for SRIT analysis. For traces shorter than 2 cm belonging to the same plane or sample, the concatenation method proposed by Labeur et al. (2024) was applied. Compaction was estimated from the maximum local height of the stylolite teeth relative to the mean baseline and ranged from 1.01 to 16 mm. L_c values ranged from 0.22 to 3.44 mm, with distributions varying among the different structures. In the Rians syncline, L_c values ranged from 1.70 to 3.44 mm, whereas values in the Mirabeau anticline and Nerthe massif ranged from 0.22 to 1.65 mm and from 0.31 to 2.49 mm, respectively (Fig. 6 and Table 1). To estimate the vertical stress from L_c, the static

Table 1
Results of inversion of BPS roughness for stress. E: Young modulus. Lc: Cross-over length. σ_V: vertical principal stress. For more details, see Supplementary Materials S5 and S6.

Structure	Site	Sample Name	Latitude	Longitude	BPS Name	Age of host rock	Length (mm)	Compaction (mm)	E (GPa)	Lc (mm)	σv (MPa)	Depth (m)*
Rians	3R	Z001	43°36′56″N	5°41′46″E	A	Maastrichtian	68.744	7.42	13	2.116	10	400
	3R	Z001	43°36′56″N	5°41′46″E	B	Maastrichtian	45.3	4.21	13	3.447	8	300
	3R	Z001	43°36′56″N	5°41′46″E	C	Maastrichtian	50.864	2.5	13	1.698	11	450
	3R	Z007	43°36′56″N	5°41′46″E	A	Maastrichtian	95.228	10.81	13	2.906	9	350
Mirabeau	7	Core_5	43°41′03″N	5°39′14″E	A	Tithonian	49.326	3.53	32	1.129	21	850
	7	Core_10	43°41′03″N	5°39′14″E	A + B + C	Tithonian	28.75	2.96	32	0.379	36	1500
	1	Z011	43°41′27″N	5°40′01″E	A	Tithonian	33.13	9.94	27	1.652	16	650
	4	Z030	43°41′22″N	5°39′41″E	Jog	Tithonian	34.75	1.86	27	0.3104	38	1500
	1	Z13A	43°41′27″N	5°40′01″E	A	Tithonian	27.648	4.2136	27	0.227	43	1750
	2	Z23	43°41′25″N	5°39′57″E	A + B + C	Tithonian	37.79	1.65	27	0.711	25	1000
	4	Z28	43°41′22″N	5°39′41″E	A	Tithonian	29.202	2.46	27	1.562	17	650
	4	Z30	43°41′22″N	5°39′41″E	A	Tithonian	51.408	3.14	27	0.327	37	1450
	4	Z30	43°41′22″N	5°39′41″E	B	Tithonian	28.29	1.72	27	0.637	27	1050
	4	Z30	43°41′22″N	5°39′41″E	C	Tithonian	27.496	2.12	27	0.447	32	1250
	11	Z55	43°41′31″N	5°39′50″E	B	Tithonian	59.432	4.09	32	1.03	21	900
	11	Z55	43°41′31″N	5°39′50″E	A + C	Tithonian	68.49	3.15	32	0.485	30	1300
	7	Z56	43°41′03″N	5°39′14″E	A	Tithonian	21.68	1.01	32	0.268	42	1750
	7	Z56	43°41′03″N	5°39′14″E	B	Tithonian	23.818	1.03	32	0.23	46	1900
	7	Z56	43°41′03″N	5°39′14″E	C	Tithonian	53.98	1.62	32	0.26	43	1800
	7	Z56	43°41′03″N	5°39′14″E	D	Tithonian	23.558	3.03	32	0.24	45	1850
	7	Z60	43°41′03″N	5°39′14″E	C	Tithonian	28.312	1.75	32	0.427	34	1400
	7	Z60	43°41′03″N	5°39′14″E	D	Tithonian	28.536	3.64	32	0.588	29	1200
	7	Z60	43°41′03″N	5°39′14″E	A	Tithonian	24.52	2.43	32	0.625	28	1150
	7	Z60	43°41′03″N	5°39′14″E	B	Tithonian	33.348	3.47	32	0.8	25	1000
	7	Z66	43°41′03″N	5°39′14″E	A	Tithonian	56.1	9.57	32	0.319	39	1600
	7	Z68-2	43°41′03″N	5°39′14″E	A	Tithonian	22.982	1.99	32	0.414	35	1400
	7	Z68-2	43°41′03″N	5°39′14″E	B + C + D	Tithonian	34.89	1.26	32	0.517	31	1250
Nerthe	1N	Z081	43°23′30″N	5°04′28″E	A	Barremian	61.318	3.69	22	0.59	24	1000
	1N	Z082	43°23′30″N	5°04′28″E	A	Barremian	66.304	3.52	22	0.378	30	1250
	1N	Z082	43°23′30″N	5°04′28″E	B	Barremian	58.888	4.1	22	0.309	33	1350
	1N	Z083	43°23′30″N	5°04′28″E	A	Barremian	66.21	7.23	22	0.446	28	1150
	1N	Z084	43°23′30″N	5°04′28″E	A'	Barremian	95.41	9	22	0.932	19	800
	1N	Z092	43°23′30″N	5°04′28″E	A'	Barremian	70.67	6.5	22	0.399	29	1200
	1N	Z093	43°23′30″N	5°04′28″E	A'	Barremian	113.2	16	22	0.701	22	900
	9N	Z151	43°19′57″N	5°05′12″E	A'	Barremian	81.31	3.24	22	0.986	19	750
	9N	Z152	43°19′57″N	5°05′12″E	A	Barremian	66.92	6.45	22	2.492	12	500
	9N	Z153	43°19′57″N	5°05′12″E	A'	Barremian	77.17	3.81	22	1.245	17	700
	9N	Z153	43°19′57″N	5°05′12″E	B'	Barremian	58.1	1.45	22	1.54	15	600
	9N	Z153	43°19′57″N	5°05′12″E	C	Barremian	51.474	2.18	22	0.462	27	1100
	9N	Z158	43°19′57″N	5°05′12″E	A + B	Barremian	71.26	5.5	22	1.423	16	650

BPS Name with a ' symbol comprise a trace concatenated from 2 cuts on the same stylolite but at different angles. * Values round to the closest multiple of 50 m.

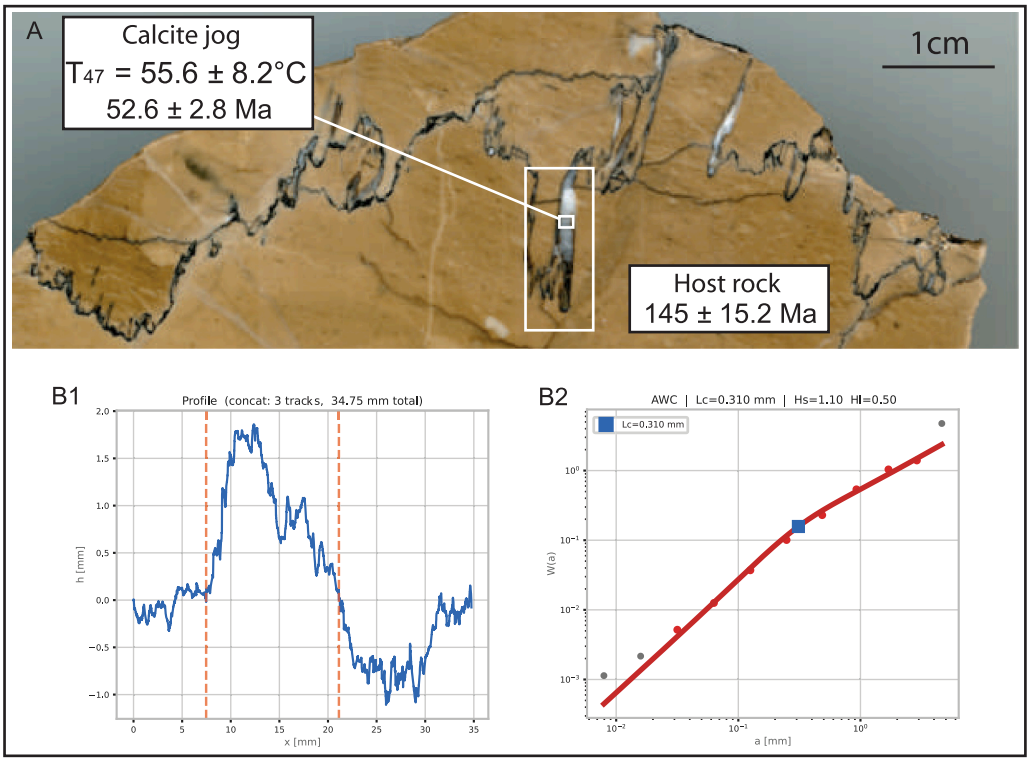


Fig. 7. A. 2D scan of the Z030 hand sample that displays the studied calcite jog (Z030-J1) linking BPS from Tithonian limestones at Mirabeau. The temperature of the fluid at the time of calcite mineralization, and the U-Pb ages of the calcite and of the host rock are given. B1: Composite 1D profile of the BPS associated with Z030-J1 jog after concatenation of three separate traces (see text and Labeur et al., 2024 for details). B2: Signal analysis of the composite profile of the BPS shown in B1 using AWC.

Young's modulus (E) was determined from Schmidt hammer measurements conducted at each sampling site. Measurements were performed at 8 sites (1 in the Rians syncline, 5 in the Mirabeau anticline, and 2 in the Nerthe massif), with a total of 10 acquisitions. Each acquisition comprised 20–50 rebound measurements performed on a flat surface. A stable rebound value was identified from the plateau reached by the mean rebound values (Supplementary Material S5). Young's modulus values calculated using Equation (2) ranged from 13 GPa for the Maastrichtian rocks to 32 GPa for the Tithonian rocks (Table 1). For a given stratigraphic age, the calculated E value was consistent among sampling sites; for example, nearly identical values (27-32) were obtained for the Tithonian rocks. The resulting E values were then used in Equation (1), together with a calcite–water interfacial energy (γ) of 0.23 J m^{-2} (Wright et al., 2001) and an average Poisson's ratio (ν) of 0.24, to calculate the magnitude of the vertical stress (σ_v). The calculated σ_v values ranged from 8 to 46 MPa (Table 1). Detailed results are provided in Supplementary Material S5 and S6.

6. Interpretation of results and discussion

6.1. Interpretation of results

6.1.1. Organic matter maturity and peak burial temperature reached by reservoir rocks

The T_{max} value of 441.5 ± 2°C places the analyzed sample from Mirabeau in the middle of the oil window. The absence of free hydrocarbons may be related to the nature of the organic matter, which is predominantly of Type III, as indicated by the hydrogen (HI) and oxygen (OI) indices of 52 mg HC/g TOC and 105 mg CO_2/g TOC, respectively. Type III organic matter generally generates relatively small amounts of hydrocarbons, which may remain largely adsorbed onto the kerogen. However, a single T_{max} value, combined with the lack of constraints on the thermal history of the sequence, does not allow the maximum temperature reached by the sample in nature to be determined precisely. Nevertheless, a temperature range of 70–90°C is considered likely (Dellisanti et al., 2010).

6.1.2. Stylolite roughness inversion and the depth of burial-related active pressure-solution

The L_c values and associated σ_v magnitudes derived from SRIT can be further used to access the depth of halt of pressure solution activity along the BPS of a given population. Using an average dry density of 2.5 g cm^{-3}, we can calculate the corresponding depths (Table 1 and Fig. 6). In the Tithonian limestones of the Mirabeau anticline, the estimated depths are distributed between 650 and 1900 m as a Gaussian centered around 1300 m. In the Maastrichtian limestones of the Rians basin, the depth values range from 300 to 450 m. In the Barremian limestones of the Nerthe massif, the distribution is bimodal, between 500 and 1350 m with two modal values of 700 m for the southern part of the Nerthe massif (Site 9N, Boumandariel) and 1100m for the northern part of the Nerthe massif (site 1N, Gueule d'Enfer) (Fig. 6). All these values are to be considered within an uncertainty of 12% (Rolland et al., 2014). For the specific case of the stylolites framing the calcite jog dated at 52.6 ± 2.8 Ma (Z030-J1, Fig. 7), the inversion of the roughness yields a depth of end of activity at 1500 ± 180 m. At the scale of individual stylolites, this depth can be considered as the depth at which pressure solution stopped, either because of local saturation, fluid overpressure or because the maximum principal stress was no longer vertical (Beaudoin et al., 2020b; Labeur et al., 2021; Lacombe et al., 2021). Considering the population of BPS, the latter explanation was invoked in various FTBs and basins to estimate the timing at which the main principal stress switched from vertical to horizontal due to increasing tectonic contraction (Labeur et al., 2021; Lacombe et al., 2021). Here, these ranges of values are used to better constrain the minimum depth at which strata were buried before contraction caused LPS-related structures, of which the timing is well constrained by U-Pb calcite

geochronology (Zeboudj et al., 2025a, 2025b).

At the first order, a difference in burial depth arises between the Rians basin, where the Maastrichtian rocks have undergone a very limited burial (~400m), the Nerthe massif where the Barremian rocks have been buried deeper (~500-1350m) and the Mirabeau anticline where the burial of the late Jurassic rocks reaches up to 1900 m. Taking into account the variability of the thickness of formations due to differential erosion and deposition from one place to another, it is difficult to test whether these differences may be simply related to the increasing age of the rocks, hence to the increasing burial from Rians to Mirabeau. Beyond regional considerations, it is interesting to note that the depth reconstructed for the Maastrichtian strata in the Rians basin is a new instance of the potential of BPS to form at shallow depth and to fingerprint the low magnitude of the vertical stress, strengthening the findings of Ebner et al. (2009) who reported a burial depth as low as 400 m determined from a BPS using SRIT.

6.2. Reconstruction of the fluid systems

6.2.1. Signatures of host rocks and fluid system during the Durancian uplift

A striking similarity in isotopic signatures is observed among the studied host rocks, spanning the Hettangian to the Barremian, although not all intervening ages are represented. Surprisingly, the $\delta^{18}O$ values of HR cements (−2‰ to −6.5‰ VPDB) are inconsistent with a Cretaceous seawater $\delta^{18}O_{fluid}$ value of −1‰ SMOW as inferred from belemnite shells (Bodin et al., 2009). Equilibrium fractionation otherwise would require precipitation at ~30°C, which is too high for seawater. One possible explanation is that the host-rock isotopic signatures were modified after deposition and no longer represent pristine seawater values. This alteration would require a regional event postdating deposition but predating most syn-kinematic calcite mineralization, with the Durancian uplift being a plausible candidate.

Godeau et al. (2018) investigated the main blocky calcite cement in the Barremian–Aptian Urgonian limestones. This sparite cement, dated at 96.7 ± 4.9 to 90.5 ± 1.6 Ma, occurs in cathodoluminescence as blotchy luminescent to non-luminescent coarse crystalline calcite (Léonide et al., 2014), suggesting precipitation from oxidizing fluids. Its stable O and C isotopic compositions range from −6‰ to −8.0‰ $\delta^{18}O$ VPDB and +1‰ to +3‰ $\delta^{13}C$ VPDB, respectively (Fig. 5B). These values are consistent with a marine carbon source and meteoric-water involvement at low to moderate temperatures (<65°C) under shallow-burial conditions (Lamarche et al., 2012; Léonide et al., 2014) (Fig. 5B). More broadly, most HR isotopic values fall within the range reported by Léonide et al. (2014) and Cochard et al. (2021) for diagenetic phases in the Urgonian limestones as a whole (+2.4‰ to −1.2‰ $\delta^{13}C$ VPDB and −3.0‰ to −10.0‰ $\delta^{18}O$ VPDB) (Fig. 5B). The Barremian host rocks from the Nerthe massif also closely match the O–C signatures of the MF2–MF3 micrites in the microporous Urgonian limestones (Léonide et al., 2014). During shallow burial, these limestones underwent micrite neomorphism in meteoric-water lenses associated with major regional exposure during the Durancian uplift, enhancing microporosity (Léonide et al., 2014). These observations support the idea of a prolonged subaerial exposure across much of Provence during the Durancian uplift. Such exposure likely promoted extensive meteoric-water circulation under humid climatic conditions and widespread bauxitization (Mondillo et al., 2025). Normal-fault activity at that time may have further enhanced fluid circulation through the porous matrix and promoted cementation (Aubert et al., 2020; Cochard et al., 2021; Corrêa et al., 2022). We therefore propose that pervasive meteoric-water ingress modified the O-isotopic signatures of most of the studied host rocks. Consistent with this interpretation, the younger host rocks deposited after the Durancian uplift (Coniacian and Maastrichtian) do not record this isotopic imprint.

In the Nerthe massif, the isotopic signatures of the calcite mineralizations dated at 110–92 Ma and associated with veins formed during the Durancian uplift (Zeboudj et al., 2025b) also cluster between −3‰ and −5‰ $\delta^{18}O$ VPDB and +1‰ and +2.2‰ $\delta^{13}C$ VPDB (Domain I; Fig. 5A), further supporting meteoric-fluid ingress during the Durancian uplift and associated extensional fracturing. This meteoric contribution is also indicated by the $\delta^{18}O_{fluid}$ value of −2.26‰ SMOW measured in sample Z224-2, dated at 90.2 ± 4.9 Ma in Mirabeau (Fig. 5C). These results are further consistent with isotopic signatures reported for calcite mineralization associated with normal faulting along the Castellas Fault (Aubert et al., 2020; Corrêa et al., 2022).

6.2.2. Fluid system during the Pyrenean shortening

Domain II encompasses the isotopic signatures of syn-kinematic calcite mineralization associated with all structures formed during Pyrenean shortening. Despite expected overlaps due to their likely continuous development (Zeboudj et al., 2025a), the structures formed during LPS, thrusting/fold growth and LSFT (see section 2.3) can be distinguished on the isotopic diagram, with a clear evolution towards less negative $\delta^{18}O$ VPDB values from LPS structures to those formed during folding and thrusting. Within the latter group, thrusts display slightly less negative $\delta^{18}O$ VPDB values than smaller-scale structures, potentially indicating more significant circulation of basinal fluids/brines during the main shortening phase. The LSFT-related structures show a similar negative range to folding-related structures, excluding thrusts. Notably, the isotopic signatures of syn-kinematic calcite from thrust zones are consistent with those reported by Aubert et al. (2020) and Corrêa et al. (2022) for calcite mineralization associated with newly formed strike-slip faults or with the reactivation of normal faults formed during the Durancian uplift (e.g., the Castellas fault) as strike-slip faults (Matonti et al., 2012) during Pyrenean shortening.

The isotopic signatures of the parent fluids during the Pyrenean shortening point towards a marine origin, an interpretation consistent with the Sr signatures of the Aptian to Campanian seawater. Fig. 8 shows the $^{87}Sr/^{86}Sr$ ratios of the 12 dated syn-kinematic calcites plotted against the McArthur et al. (2012) reference curve, either as a function of host-rock age or the U-Pb age of the mineralization. Values plotting on the curve may indicate either mobilization of connate fluids from the local host rock or precipitation from seawater at the time of calcite mineralization. Values above or below the curve are inconsistent with precipitation from seawater at the time the host rock was deposited (if marine) or the calcite precipitated. In detail, sample Z103-1 possibly recorded the precipitation of connate fluids that were remobilized during the Pyrenean-related fracture opening. Samples Z169-2, Z155, Z126 and Z132-C likely recorded the downward migration of Campanian seawater coeval to the opening of the fractures, while Z203 recorded a similar phenomenon but during the Eocene. The interpretation of other samples, that have $^{87}Sr/^{86}Sr$ ratios consistent with Cretaceous seawater but lower than the seawater at the time of their precipitation, is ambiguous if solely based on the $^{87}Sr/^{86}Sr$ ratios. The combination with clumped isotopes and derived $\delta^{18}O_{fluid}$ values resolves this ambiguity. Samples Z043, Z015b, Z189-1a show $\delta^{18}O_{fluid}$ isotopic signatures in favor of a downward meteoric fluid migration and subsequent calcite precipitation in fractures within Tithonian (Z043, Z015b) and Barremian (Z189-1a) rocks, during the Campanian (Z189-1a) and Eocene (Z043, Z015b) times, i.e., during the Pyrenean shortening. The interpretation of sample Z071-2 is not straightforward as no $\delta^{18}O_{fluid}$ value was measured, yet it could be interpreted like Z207 by a mixing between Mesozoic seawater and Cenozoic meteoric fluids. Despite the absence of $^{87}Sr/^{86}Sr$ data, the $\delta^{18}O_{fluid}$ values of samples Z136.1, Z225 and Z023-1b also support a meteoric contribution to the fluids precipitating

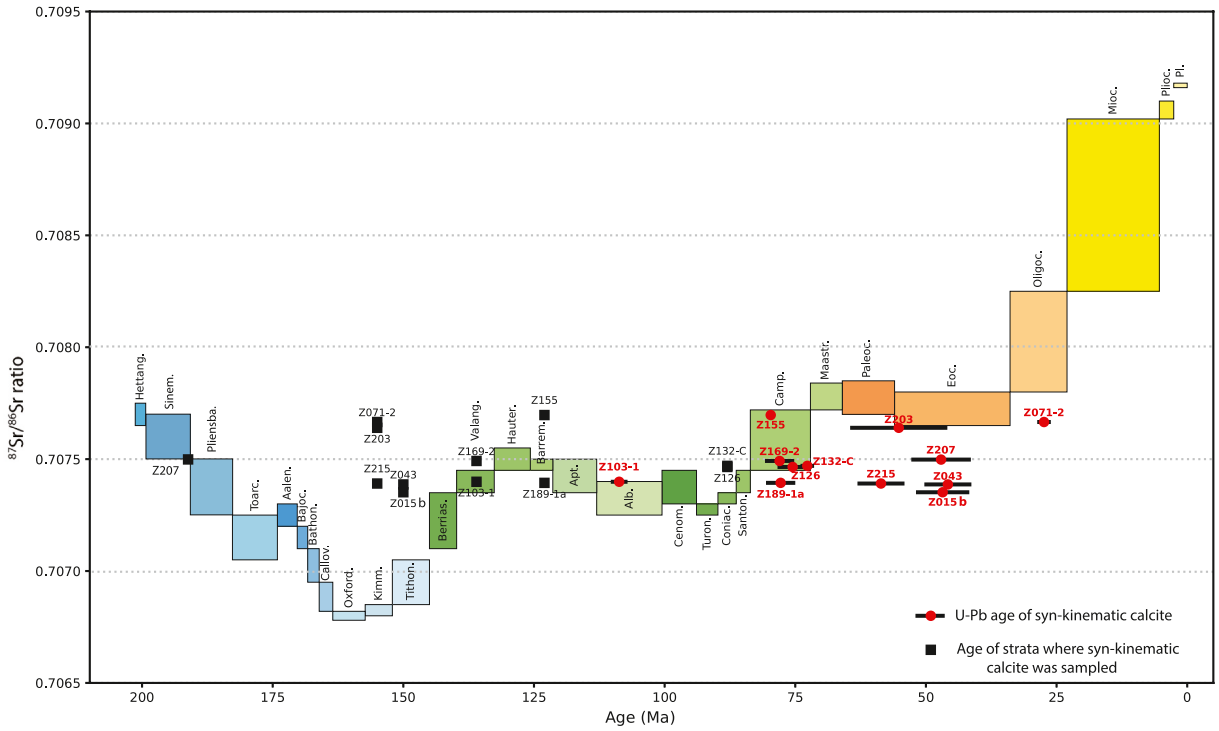


Fig. 8. $^{87}Sr/^{86}Sr$ ratios of syn-kinematic calcite mineralizations reported as a function of the U-Pb age of the calcites and the age of the host rocks, projected onto the $^{87}Sr/^{86}Sr$ ratios versus time curve constructed using the ranges reported in MacArthur et al. (2012), and the international stratigraphic chart color code. In red circles are reported the sample's mineralization at the precipitation time (obtained with U-Pb geochronology) and in black squares are reported the same sample's mineralization but at the age of the strata they were sampled from. (For interpretation of the references to color in this figure legend, the reader is referred to the Web version of this article.)

syn-kinematic calcite.

Clumped isotope signatures further indicate that the fluids precipitating syn-kinematic calcite were generally hotter during LPS (56-74°C) than during folding and thrusting (50-55°C) (Fig. 5C), while displaying comparable $\delta^{18}O_{fluid}$ ratios, consistent with a semi-closed system in which marine fluids mixed with meteoric fluids. This thermal evolution may reflect either a change in the geothermal gradient or, more likely, progressive rock exhumation during ongoing Pyrenean shortening.

In summary, the fluid system during the Pyrenean shortening was presumably semi-closed, with potential ingress of meteoric fluids, particularly during LPS. This contrasts with most paleofluid reconstructions in folded structures (e.g., Beaudoin et al., 2011, 2015; Beaudoin et al., 2020a; Evans and Fischer, 2012; Berio et al., 2022; see synthesis in Beaudoin et al., 2022) which generally document a compartmentalized, closed fluid system during LPS, followed by opening to surficial meteoric fluids or hydrothermal fluids during folding and thrusting.

Finally, the range of $^{87}Sr/^{86}Sr$ ratios across all samples also rules out contributions from radiogenic rocks (e.g., crystalline basement) or basement-derived rocks (e.g., early Triassic sandstones), indicating that the parent fluids did not circulate at depth near or within these rocks. This implies either shallow rooting of the sampled Pyrenean thrusts within the Middle–Late Triassic evaporites and limited basement-involved shortening, or an efficient impermeable barrier effect of these evaporites against potentially ascending basement-derived fluids.

6.2.3. *Fluid system during the post-Pyrenean rifting events*

The few calcite samples collected from veins attributed either to the Oligocene E–W extension (WER) or the Oligo-Miocene NNW–SSE extension (LPR) display distinct isotopic signatures (Domain III in Fig. 5A), particularly in $\delta^{13}C$ VPDB. Their more negative $\delta^{13}C$ values may reflect an increasing contribution of meteoric fluids, combined with soil-derived or bacterially influenced carbon. This enhanced meteoric contribution is consistent with the more negative $\delta^{13}C$ signatures of the latest sparite cement (Oligo-Miocene) in the Urgonian limestones (C5, Cochard et al., 2021), as well as diagenetic evidence for subaerial environments in the Nerthe massif during Oligo-Miocene times (Zeboudj et al., 2025b). Despite the limited dataset, these results suggest that the fluid system differed from that involved during Pyrenean shortening, reflecting the change in the geodynamic evolution of Provence from Pyrenean shortening to Oligo-Miocene extensions. Further work is needed to test this hypothesis and better characterize the fluid system associated with the post-Pyrenean rifting events.

6.3. *Reconstructing the depth-T-d-t paths of late Jurassic and Cretaceous host rocks using the multi-proxy approach: comparison with published literature and discussion*

The isotopic dataset highlights several syn-kinematic calcite mineralizations that can be used to reconstruct local geothermal temperatures, following the workflow described in section 4. These calcites precipitated at temperatures determined using T_{47} and at times constrained by U/Pb geochronology. To assess whether these syn-kinematic calcites precipitated under thermal equilibrium with their host rocks, we considered two criteria that must be fulfilled. The first is that the fluid source, constrained by a combination of the $^{87}Sr/^{86}Sr$ ratio and $\delta^{18}O_{fluid}$, should indicate the downward migration of either meteoric fluid or connate fluid sourced from a rock stratigraphically younger than the rock hosting the mineralized fracture. The second is that the fluid/rock ratio must be sufficiently low to prevent the fluid temperature from differing significantly from that of the host rock. In other words, we consider that when the fluid input is limited and local fluid–rock interaction is extensive, the precipitation temperature reflects the local geothermal temperature. The second criterion can be assessed by examining the degree to which the calcite mineralization is geochemically buffered by the host rock. We assume that geochemical buffering of

the calcite indicates a low fluid/rock ratio at the time of precipitation, such that the fluid is presumably also thermally buffered by the host rock. To assess the extent of fluid–rock interaction and define the buffered domain geochemically, we plotted the differences in $\delta^{13}C$ VPDB and $\delta^{18}O$ VPDB between the calcite mineralization and the surrounding host rock (Fig. 5D). Assuming that the variability in $\delta^{13}C$ VPDB and $\delta^{18}O$ VPDB values among host rocks of a given age reflects small-scale isotopic heterogeneities, the buffered domain can be approximately defined as a rectangle corresponding to vein–host-rock differences of 2‰ in $\delta^{13}C$ and 3‰ in $\delta^{18}O$ (Fig. 5D). This conservative approach resulted in narrowing our dataset, with only 5 samples having $\delta^{13}C$ and $\delta^{18}O$ signatures falling within this buffered domain: 3 samples at

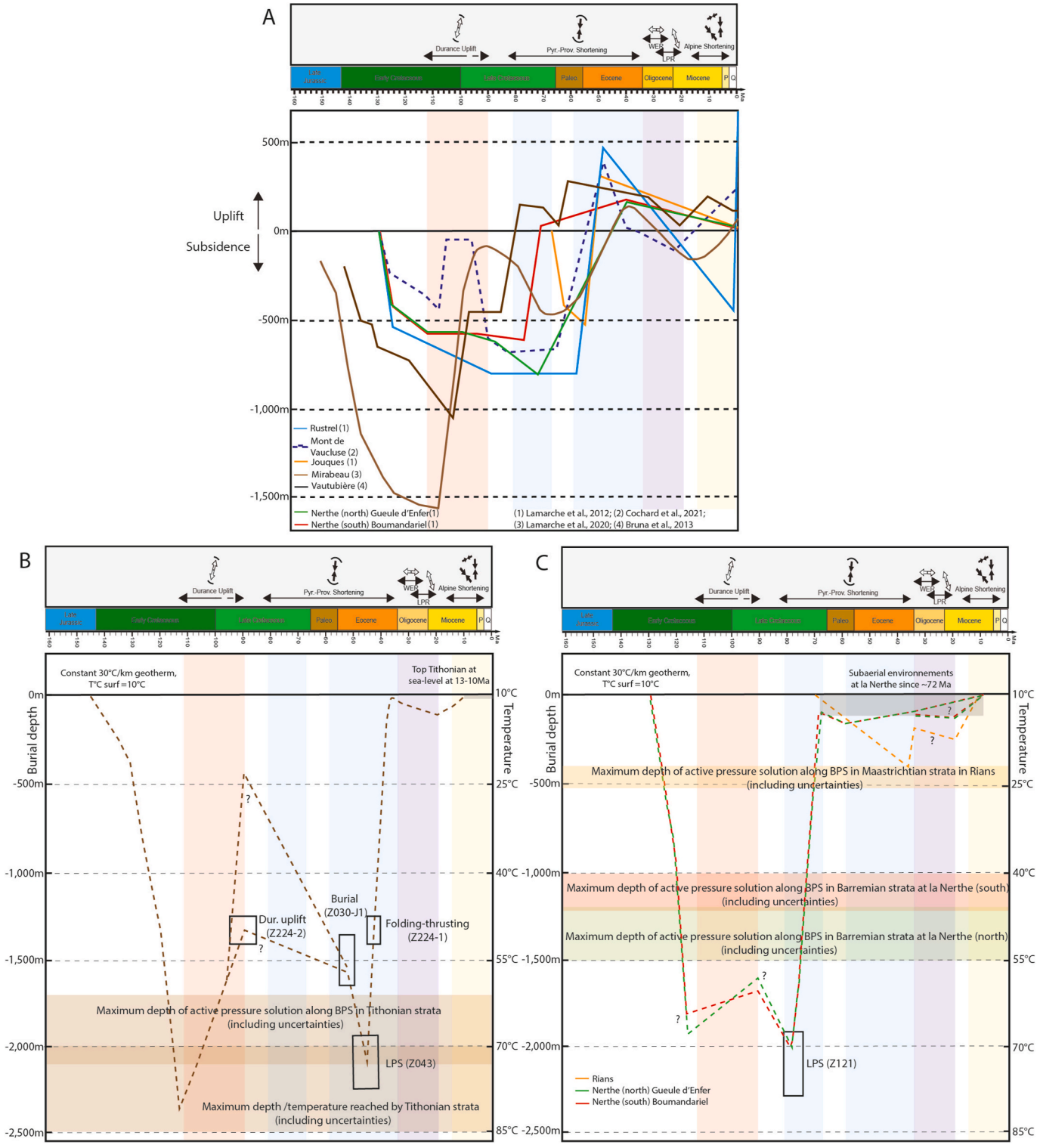


Fig. 9. A: Published subsidence/uplift curves for different localities and age of rocks in Provence. B: Burial curve reconstructed for the Tithonian rocks in the Mirabeau anticline. C: Burial curves reconstructed for the Barremian rocks in the Nerthe massif (north/south) and for Maastrichtian rocks in the Rians syncline. The black frames represent the anchor points (with uncertainties on temperature and age) reconstructed from the geochemical analysis of the syn-kinematic mineralization.

Mirabeau, Z043 (45.8 ± 4.5 Ma, 73.51 ± 4.9°C), Z224-1 (42.4 ± 2.4 Ma, 51.61 ± 3.9°C), and Z224-2 (90.2 ± 4.9 Ma, 51.5 ± 3.8°C); 1 sample at la Nerthe, Z121 (78.4 ± 1.9 Ma, 73.6 ± 5.4°C) and 1 sample at Bimont, Z215 (58.6 ± 4.5 Ma, 51.1 ± 4.4°C). Finally, at Mirabeau, a stylolite jog, of which the local origin cannot be argued against, provided simultaneously independent constraints on depth, temperature and age (Z030-J1: 52.6 ± 2.8 Ma, 55.6 ± 8.2°C, 1500 ± 180 m; Fig. 7).

Fig. 9B shows the burial history of the Tithonian strata at the Mirabeau anticline. The burial-time curve is constrained by (1) the T–t anchor point provided by a vein formed during the Durancian uplift (Z224-2), the depth–T–t anchor point provided by the BPS-related calcite jog (sample Z030-J1), and the T–t anchor points provided by a mineralized mesoscale fault formed during LPS (Z043) and a vein formed during folding (Z224-1); (2) the maximum temperature reached by the Tithonian strata, constrained by Rock-Eval thermometry; (3) the minimum burial depth inferred from inversion of BPS roughness; (4) the likely limited burial of the fold during Oligo-Miocene extension; and (5) the unconformable deposition of marine Miocene strata over the older formations. We considered a constant geothermal gradient of 30 °C/km and a surface temperature of 10°C. This value is consistent with the depth-T constraints provided by sample Z030-J1, which indicate a temperature of ~55°C at a depth of ~1500 m at ~53 Ma. Assuming a surface temperature of 10°C, these values correspond to a geothermal gradient of ~30 °C/km. Paleogeothermal gradients were also reconstructed for the inverted hyperextended rift basin of the western Pyrenees by Saspiturry et al. (2020). The estimated gradients vary systematically with structural position across the Albian–Cenomanian rift, from ~34 °C/km in the European proximal margin to ~37–47 °C/km in the necking zones and ~57–60 °C/km in the hyperextended domain. Although these gradients are inherited from the thermal regime established during Albian–Cenomanian rifting, Saspiturry et al. (2020) suggest that the maximum paleogeothermal gradients were probably reached during the Paleocene–early Eocene. Since the domains investigated in Provence are broadly analogous to the European proximal margin domain of the pre-Pyrenean rift, the ~30 °C/km adopted here provides a reasonable first-order approximation of the geothermal gradient in Provence during the Late Cretaceous–Eocene. For the post-Pyrenean extensional stages, we also retained a geothermal gradient of ~30 °C/km as a first-order modelling assumption because the structural position of Provence was again analogous to a proximal margin domain during the Oligocene–Miocene extensions associated with the West European and Liguro-Provençal rift systems; however, it should be regarded as a simplifying assumption for this latter period rather than as a directly constrained value.

Although direct comparison with published subsidence–uplift curves for Mirabeau and the nearby Vautubière anticline (Bruna et al., 2013; Lamarche et al., 2020, Fig. 9A) is not straightforward, our results suggest (1) a greater initial burial depth of the Tithonian strata before the Durancian uplift, reaching 2000–2500 m; (2) significant reburial during the Late Cretaceous; and (3) greater exhumation during the second (Eocene) phase of Pyrenean shortening in Provence, estimated at ~2000 m from sample Z043, assuming that LPS occurred at nearly peak burial at 45.8 ± 4.5 Ma. The main uncertainty concerns the amount of exhumation associated with the Durancian uplift. A conservative estimate is ~1000 m (from ~2200–2500 m to ~1300–1500 m), with the anchor point representing the minimum burial depth of the Tithonian strata at that time. Alternatively, if the anchor point is considered to constrain only the path to the surface, if the extensional veins formed at a depth of 1300 m through fluid-assisted fracturing, and if the Mirabeau anticline was located near the apex of the Durancian high, an additional ~800 m of exhumation may be inferred, provided that Berriasian to Hauterivian rocks remained preserved in the fold limbs. Notably, the burial and erosional exhumation of the Tithonian strata inferred here exceed the commonly accepted estimates of 700–1000 m and 500–800 m of Mesozoic limestones removed during the Durancian uplift and the Pyrenean shortening, respectively.

Fig. 9C shows the tentative burial history of the Maastrichtian strata in the Rians syncline. The curve is constrained by (1) the minimum burial depth inferred from inversion of BPS roughness, although the dataset is very limited; (2) the late record of N–S shortening at ~36 Ma in the syncline (Zeboudj et al., 2025b); and (3) the unconformable deposition of marine Miocene strata at nearby localities in the basin. As for Mirabeau, we adopted a constant geothermal gradient of 30 °C/km and a surface temperature of 10°C. Considering the uncertainties, the order of magnitude of the burial depth inferred from BPS roughness inversion is consistent with the estimated thickness of the overlying Paleocene–Eocene formations (~200 m) and with the conclusions of Balansa et al. (2022). Fig. 9C also shows the burial history of the Barremian strata in the northern and southern Nerthe massif. The first constraint is the unique T–t anchor point provided by sample Z121, a nearly bed-perpendicular vein formed during Pyrenean LPS (Fig. 3F). Although the rock hosting this vein was subsequently overthrust and thus tectonically buried during the main folding and thrusting phase (Zeboudj et al., 2025b, Fig. 3G), the formation of this vein during LPS, as indicated by its attitude relative to bedding and its U-Pb age, implies that no tectonic loading was superimposed on the original sedimentary load at this time. The reconstructed depth therefore represents pristine (stratigraphic) burial. The other constraints are (1) the minimum burial depth inferred from inversion of BPS roughness; (2) evidence for diagenetic cementation under subaerial conditions from the onset of thrust activity (~72 Ma) to the Miocene (~9.5 Ma), suggesting that the range was close to emersion soon after it started to form (Zeboudj et al., 2025b); (3) the limited erosion associated with the Durancian uplift, as Barremian–Aptian Urgonian limestones are still preserved; and (4) the unconformable deposition of marine Miocene strata over the older formations. Compared with published subsidence–uplift curves (Lamarche et al., 2012; Lavenu et al., 2013, Fig. 9A), our results indicate substantially greater burial of the Barremian strata than previously estimated (maximum overburden of 600 m at Boumandariel and 900 m at Gueule d'Enfer according to the stratigraphic logs of Lavenu et al., 2013). Despite this greater overall burial, SRIT consistently indicates greater burial depths for Barremian strata in Gueule d'Enfer than in Boumandariel. Our results also reveal a greater amount (~2000 m) of rocks that were eroded away during the Pyrenean shortening, mainly during the paroxysmal late Cretaceous phase.

From a methodological point of view, our approach is fundamentally different from those previously adopted to quantify the vertical movements of strata (subsidence and uplift) in Provence. In addition to inconsistencies among these models, the subsidence–uplift models shown in Fig. 9A, which do not explicitly reconstruct burial as a function of time, rely primarily on 1D Airy backstripping of sedimentary strata and on estimates of eroded thicknesses derived either from comparisons with nearby localities where the corresponding strata are preserved or from borehole data, and/or from geometrical estimates based on balanced cross sections, without using paleo-thermobarometric constraints to independently quantify paleoburial and/or paleotemperature (e.g., Roure et al., 2010). By contrast, the rationale underlying our approach is to reconstruct quantitatively and, as far as possible, independently, the depth and temperature at which strata were buried or fractures formed at specific stages of their geological history, as constrained by calcite geochronology. We achieve this by combining a geochemical toolbox with paleopiezometric constraints and first-order geological constraints. This approach yields internally consistent estimates of burial and exhumation that do not require a priori assumptions about the initial thickness of the sedimentary succession or the amount of erosion. It therefore provides a new and promising tool with broad applicability to reconstruct the burial and deformation histories of carbonate reservoir rocks worldwide.

The approach nevertheless has several important limitations. First, it requires a sufficiently large and robust set of U–Pb ages covering the main stages of the tectonic history. Second, it is affected by the intrinsic uncertainties associated with the paleothermometric and

paleopiezometric techniques employed. Third, it requires mineralizing fluids to have been sufficiently close to thermal equilibrium with their host rocks for fluid temperatures to be used as constraints on rock temperature; this requirement inevitably restricts the number of suitable samples. Fourth, converting temperature into burial depth requires an assumption about the geothermal gradient, which may have varied through time. Here, we assumed a constant geothermal gradient of ~30 °C/km, which appears reasonable for the entire geological history investigated. Since our aim is to provide estimates of burial and exhumation depths rather than values with unwarranted precision, we did not consider alternative geothermal gradients. These would be poorly constrained in any case, and moderate variations in the geothermal gradient would not affect our main conclusions.

If our interpretations are correct, they call for a re-evaluation of two aspects of the geological history of Provence. First, they may require reassessment of previous estimates of sedimentary formation thicknesses based on comparisons with localities where the eroded strata are preserved, or on estimates of eroded rock volumes derived from balanced cross sections. Such approaches may implicitly assume laterally uniform depositional conditions and may therefore overlook local controls on anomalously thick or thin sediment accumulation, such as fault-controlled depocenters or subsequent tectonic modification. Second, our results raise questions about the fate of the eroded material in terms of mass balance and about the relative importance of carbonate dissolution versus physical erosion during periods of uplift, particularly under subaerial conditions and in a warm, humid climate such as that prevailing during the Durancian uplift. Further investigations are required to fully test and establish the robustness and broader applicability of our new approach.

7. Conclusions

In this study, we use syn-kinematic calcite mineralization associated with a wide spectrum of structures (large-scale thrusts, veins, mesoscale faults, and stylolite jogs) to reconstruct (1) the nature, temperature, and origin of the fluids present during the tectonic evolution of Provence, and (2) to constrain in a novel way the depth–temperature–deformation–time evolution of these strata.

First, the fluid system appears to have varied substantially between successive tectonic events. A significant imprint of meteoric water is documented during the 'mid'-Cretaceous Durancian uplift and associated extensional deformation. In contrast, the fluid system appears to have remained semi-closed during the Late Cretaceous–Eocene Pyrenean shortening, with mixing between marine and meteoric fluids occurring to varying degrees depending on the deformation substage (LPS, folding–thrusting stage, LSFT) and the scale of the structures investigated (mesostructures versus major fault zones). Although constrained by only a limited number of data, the fluid system associated with the subsequent Oligocene and Oligo-Miocene extensional events also appears to have differed significantly from those of the preceding tectonic stages.

Second, we propose an original workflow that integrates structural, geochemical, paleopiezometric and geochronological constraints to reconstruct quantitative depth–temperature–deformation–time anchor points, with the aim of deriving burial–time curves for the Late Jurassic and Early to Late Cretaceous carbonate host rocks of Provence. This workflow involves the selection of relevant structural objects and associated syn-tectonic calcite mineralization, ensuring that the mineralizing fluid was at, or close to, thermal equilibrium with the host rock, while the timing of mineral precipitation is independently constrained by U–Pb geochronology. This approach provides an alternative to conventional subsidence–uplift models based on backstripping of strata from well logs and outcrops, combined with structural geometries derived primarily from balanced cross-sections previously published for Provence. Comparison between our burial–time models and previously published subsidence–uplift histories indicates that the burial depths reconstructed using a geochemistry-assisted structural geology approach are substantially greater than previously estimated. This discrepancy challenges the previously proposed regional picture of vertical strata movements.

Beyond the regional implications, this preliminary case study illustrates how the integrated study of deformation and geochemical processes, when embedded within a fully time- and depth-calibrated framework, can provide a powerful and transferable approach for better constraining the large-scale geological evolution of fold-and-thrust belts and sedimentary basins.

CRediT authorship contribution statement

Olivier Lacombe: Writing – original draft, Visualization, Validation, Supervision, Resources, Project administration, Methodology, Investigation, Funding acquisition, Formal analysis, Data curation, Conceptualization. **Nicolas E. Beaudoin:** Writing – review & editing, Visualization, Validation, Supervision, Software, Resources, Methodology, Investigation, Formal analysis, Data curation, Conceptualization. **Anies Zeboudj:** Investigation, Formal analysis. **Juliette Lamarche:** Investigation. **Jean-Paul Callot:** Writing – review & editing, Validation, Investigation. **Laurent Emmanuel:** Writing – review & editing, Methodology, Formal analysis. **Mathieu Daeron:** Writing – review & editing, Methodology, Formal analysis. **Nicolas Espurt:** Writing – review & editing, Validation. **Sidonie Revillon:** Writing – review & editing, Formal analysis, Methodology.

Declaration of competing interest

The authors declare that they have no known competing financial interests or personal relationships that could have appeared to influence the work reported in this paper.

Acknowledgements

Rock-Eval analyses were carried out with the AMOS facility of OSU Ecce Terra of Sorbonne Université. François Baudin is warmly thanked for his help during data acquisition and interpretation. Comments by reviewers Stephen Cox and Luigi Berio helped improve the clarity of the manuscript. This study received no specific funding.

Appendix A. Supplementary data

Supplementary data to this article can be found online at https://doi.org/10.1016/j.jsg.2026.105846.

Data availability

Data will be made available on request.

References

Advokaat, E.L., van Hinsbergen, D.J.J., Maffione, M., Langereis, C.G., Vissers, R.L.M., Cherchi, A., Schroeder, R., Madani, H., Columbu, S., 2014. Eocene rotation of Sardinia, and the paleogeography of the western Mediterranean region. Earth Planet Sci. Lett. 401, 183–195.

Agosta, F., Luetkemeyer, P.B., Lamarche, J., Crider, J.G., Lacombe, O., 2016. Special issue: "the role of fluids in faulting and fracturing in carbonates and other upper crustal rocks". Tectonophysics 690 (part A), 1–3.

Aharonov, E., Karcz, Z., 2019. How stylolite tips crack rocks. J. Struct. Geol. 118, 299–307.

Ahmadhadi, F., Daniel, J.M., Azzizadeh, M., Lacombe, O., 2008. Evidence for pre-folding vein development in the Oligo-Miocene Asmari Formation in the Central Zagros Fold Belt, Iran. Tectonics 27, TC1016.

Andreani, L., Loget, N., Rangin, C., Le Pichon, X., 2010. New structural constraints on the Southern Provence thrust belt (France): evidence for an eocene shortening event linked to the Corsica-Sardinia subduction. Bull. Soc. Geol. Fr. 181, 547–563.

Angrand, P., Mouthereau, F., 2021. Evolution of the alpine orogenic belts in the western mediterranean region as resolved by the kinematics of the Europe-Africa diffuse plate boundary. BSGF-Earth Sci. Bulletin 192, 42, 2021.

Arthaud, F., Mattauer, M., 1969. Exemples de stylolites d'origine tectonique dans le Languedoc, leurs relations avec la tectonique cassante. Bull. Soc. Geol. Fr. 7 (5), 738–744.
Arthaud, F., Seguret, M., 1981. Les structures pyreneennes du Languedoc et du Golfe du Lion (Sud de la France). Bull. Soc. Geol. Fr. S7-XXIII, 51–63.
Aubert, I., Lamarche, J., Léonide, P., 2019. Deciphering background fractures from damage fractures in fault zones and their effect on reservoir properties in microporous carbonates (Urgonian limestones, SE France). Pet. Geosci. 25, 443–453.
Aubert, I., Léonide, P., Lamarche, J., Salardon, R., 2020. Diagenetic evolution of fault zones in urgonian microporous carbonates, impact on reservoir properties (Provence—Southeast France). Solid Earth 11, 1163–1186.
Aydin, A., Basu, A., 2005. The Schmidt hammer in rock material characterization. Eng. Geol. 81 (1), 1–14.
Bah, B., Beaudoin, N.E., Lacombe, O., Girard, J.P., Gout, G., Godeau, N., Deschamps, P., 2023b. Multi-proxy reconstruction of the burial history and porosity evolution of the TOCA carbonate formation in the Lower Congo Basin (South West Africa). Mar. Petrol. Geol. 148, 106018.
Bah, B., Lacombe, O., Beaudoin, N.E., Teboul, P.A., Girard, J.P., Gout, C., 2024. Paleostress evolution of the Outer Kwanza basin (offshore Angola); comparison with the Congo basin and implications for the tectonic history of the Central segment of the West Africa passive margin. J. Afr. Earth. Sci. 218, 105382.
Bah, B., Lacombe, O., Beaudoin, N.E., Zeboudj, A., Gout, C., Girard, J.-P., Teboul, P.-A., 2023a. Paleostress evolution of the West Africa passive margin: new insights from calcite twinning paleopiezometry in the deeply buried syn-rift TOCA formation (Lower Congo Basin). Tectonophysics 863, 229997.
Balansa, J., Espurt, N., Hippolyte, J.-C., Philip, J., Caritg, S., 2022. Structural evolution of the superimposed provençal and subalpine fold-thrust belts (SE France). Earth Sci. Rev. 227, 103972, 2022.
Barbier, M., Hamon, Y., Callot, J.P., Floquet, M., Daniel, J.M., 2012. Sedimentary and diagenetic controls on the multiscale fracturing pattern of a carbonate reservoir: the Madison Formation (Sheep Mountain, Wyoming, USA). Mar. Petrol. Geol. 29 (1), 50–67.
Baroux, E., 2000. Tectonique Active En Région À Sismicité Modérée: Le Cas De La Provence (France): Apport D'Une Approche Pluridisciplinaire. Unpublished Ph.D. Thesis, Université Paris, Paris, France.
Baroux, E., Béthoux, N., Bellier, O., 2001. Analyses of the stress field in southeastern France from earthquake focal mechanisms. Geophys. J. Int. 145, 336–348.
Bauer, J.F., Krumbholz, M., Meier, S., Tanner, D.C., 2017. Predictability of properties of a fractured geothermal reservoir: the opportunities and limitations of an outcrop analogue study. Geotherm. Energy 5 (1), 24.
Beaudoin, N., Bellahsen, N., Lacombe, O., Emmanuel, L., 2011. Fracture-controlled paleohydrogeology in a basement-cored, fault-related fold: Sheep Mountain anticline (Wyoming, USA). G-cubed 12, Q06011.
Beaudoin, N., Bellahsen, N., Lacombe, O., Emmanuel, L., Pironon, J., 2014. Crustal-scale fluid flow during the tectonic evolution of the Bighorn Basin (Wyoming, USA). Basin Res. 26, 403–435.
Beaudoin, N., Gasparrini, M., David, M.E., Lacombe, O., Koehn, D., 2019. Bedding-parallel stylolites as a tool to unravel maximum burial depth in sedimentary basins: application to Middle Jurassic carbonate reservoirs in the Paris basin. Geol. Soc. Am. Bull. 131 (7/8), 1239–1254.
Beaudoin, N., Huyghe, D., Bellahsen, N., Lacombe, O., Emmanuel, L., Mouthereau, F., Ouahnon, L., 2015. Fluid systems and fracture development during syn-depositional fold growth : example from the Pico del Aguila Anticline, Sierras Exteriores, Southern Pyrenees, Spain. J. Struct. Geol. 70, 23–38.
Beaudoin, N., Koehn, D., Lacombe, O., Lecouty, A., Billi, A., Aharonov, E., Parlangeau, C., 2016. Fingerprinting stress: stylolite and calcite twinning paleopiezometry revealing the complexity of progressive stress patterns during folding—the case of the monte nero anticline in the apennines, Italy. Tectonics 35, 1687–1712.
Beaudoin, N., Lacombe, O., 2018. Recent and future trends in paleopiezometry in the diagenetic domain: insights into the tectonic paleostress and burial depth history of fold-and-thrust belts and sedimentary basins. J. Struct. Geol. 114, 357–365.
Beaudoin, N., Lacombe, O., Bellahsen, N., Emmanuel, L., 2013. Contribution of studies of sub-seismic fracture populations to paleo-hydrological reconstructions (Bighorn Basin, USA). Procedia Earth and Planetary Science, Water Rock Interaction 14 (7), 57–60.
Beaudoin, N., Lacombe, O., Hoareau, G., Callot, J.P., 2022. How the geochemistry of syn-kinematic calcite cements depicts past fluid flow and assists structural interpretations : a review of concepts and applications in orogenic forelands. Geol. Mag. 159, 11–12, 2157-2219.
Beaudoin, N., Lacombe, O., Koehn, D., David, M.E., Farrell, N., Healy, D., 2020b. Vertical stress history and paleoburial in foreland basins unravelled by stylolite roughness paleopiezometry : insights from bedding-parallel stylolites in the Bighorn Basin (Wyoming, USA). J. Struct. Geol. 136, 104061.
Beaudoin, N., Lacombe, O., Roberts, N.M.W., Koehn, D., 2018. U-Pb dating of calcite veins reveals complex stress evolution and thrust sequence in the Bighorn Basin, USA. Geology 46 (11), 1015–1018.
Beaudoin, N.E., Koehn, D., Aharonov, E., Billi, A., Daeron, M., Boyce, A., 2025. Reconstruction of the temperature conditions of burial-related pressure solution by clumped isotopes validates the analysis of sedimentary stylolites roughness as a reliable depth gauge. Minerals 15, 73, 2025.
Beaudoin, N.E., Labeur, A., Lacombe, O., Koehn, D., Billi, A., Hoareau, G., Boyce, A., John, C.M., Marchegiano, M., Roberts, N.M., et al., 2020a. Regional-scale paleofluid system across the Tuscan nappe–umbria–marche Apennine Ridge (Northern Apennines) as revealed by mesostructural and isotopic analyses of stylolite–vein networks. Solid Earth 11, 1617–1641.
Behar, F., Beaumont, V., De, B., Penteado, H.L., 2001. Rock-Eval 6 technology: performances and developments. Oil Gas Sci. Technol. 56, 111–134. Revue de l'Institut Français du Pétrole.
Benedicto, A., Schultz, R.A., 2010. Stylolites in limestone: magnitude of contractional strain accommodated and scaling relationships. J. Struct. Geol. 32, 1250–1256.
Bergerat, F., 1987. Stress fields in the European platform at the time of Africa-Eurasia collision. Tectonics 6, 99–132.
Berio, L.R., Mittempergher, S., Storti, F., Bernasconi, S.M., Cipriani, A., Lugli, F., Balsamo, F., 2022. Open–closed–open palaeofluid system conditions recorded in the tectonic vein networks of the Parmelan anticline (Bornes Massif, France). J. Geol. Soc. 179 (5), jgs2021–j2117.
Bernasconi, S.M., Daëron, M., Bergmann, K.D., Bonifacie, M., Meckler, A.N., Affek, H.P., Anderson, N., Bajnai, D., Barkan, E., Beverly, E., et al., 2021. InterCarb: a community effort to improve interlaboratory standardization of the carbonate clumped isotope thermometer using carbonate standards. G-cubed 22, e2020GC009588.
Bernasconi, S.M., Müller, I.A., Bergmann, K.D., Breitenbach, S.F.M., Fernandez, A., Hodell, D.A., Meckler, A.N., Millan, I., Ziegler, M., 2018. Reducing uncertainties in carbonate clumped isotope analysis through consistent carbonate-based standardization. G-cubed 19, 2895–2914.
Berra, F., Carminati, E., 2012. Differential compaction and early rock fracturing in high-relief carbonate platforms: numerical modelling of a Triassic case study (Esino Limestone, Central Southern Alps, Italy). Basin Res. 24 (5), 598–614.
Bertotti, G., de Graaf, S., Bisdom, K., Oskam, B., Vonhof, H.B., Bezerra, F.H., Reijmer, J.J. G., Cazarin, C.L., 2017. Fracturing and fluid-flow during post-rift subsidence in carbonates of the Jandaíra Formation, Potiguar Basin, NE Brazil. Basin Res. 29 (6), 836–853.
Besson, D., 2005. Architecture Du Bassin rhodano-provençal Miocène (Alpes, SE France): Relations Entre Déformation, Physiographie Et Sédimentation Dans Un Bassin Molassique d'avant-pays. Ecole Nationale Supérieure des Mines de Paris. Unpublished PhD.
Bestani, L., Espurt, N., Lamarche, J., Bellier, O., Hollender, F., 2015. Reconstruction of the Provence chain evolution, Southeastern France. Tectonics 35, 1506–1525.
Bestani, L., Espurt, N., Lamarche, J., Floquet, M., Philip, J., Bellier, O., Hollender, F., 2016. Structural style and evolution of the Pyrenean-Provence thrust belt, SE France. Bull. Soc. Geol. Fr. 186, 223–241.
Blès, J.L., Gros, Y., 1991. Stress field changes in the Rhone Valley from the Miocene to the present. Tectonophysics 194 (3), 265–277.
Bodin, S., Fiet, N., Godet, A., Matera, V., Westermann, S., Clément, A., Janssen, N.M.M., Stille, P., Föllmi, K.B., 2009. Early Cretaceous (late Berriasian to early Aptian) palaeoceanographic change along the northwestern Tethyan margin (Vocontian Trough, southeastern France): $\delta^{13}C$, $\delta^{18}O$ and Sr-isotope belemnite and whole-rock records. Cretac. Res. 30 (5), 1247–1262.
Boschetti, L., Rolland, Y., Mouthereau, F., Schwartz, S., Milesi, G., Munch, P., Bernet, M., Balvay, M., Thiéblemont, D., Bonno, M., Martin, C., Monié, P., 2025. Thermochronology of the Maures-Tanneron crystalline basement: insights for SW Europe Triassic to Miocene tectonic history. Swiss J. Geosci. 118 (1), 14.
Brigaud, B., Bonifacie, M., Pagel, M., Blaise, T., Calmels, D., Haurine, F., Landrein, P., 2020. Past hot fluid flows in limestones detected by Δ_{47}–(U-Pb) and not recorded by other geothermometers. Geology 48 (9), 851–856.
Bruna, P.O., Guglielmi, Y., Lamarche, J., Floquet, M., Fournier, F., Sizun, J.P., Gallois, A., Marié, L., Bertrand, C., Hollender, F., 2013. Porosity gain and loss in unconventional reservoirs: example of rock typing in Lower Cretaceous hemipelagic limestones, SE France (Provence). Mar. Petrol. Geol. 48, 186–205.
Champion, C., Choukroune, P., Clauzon, G., 2000. La déformation post-Miocène en Provence Occidentale. Geodin. Acta 13, 67–85.
Chen, J., Guo, X., Tao, Z., Cao, Z., Wang, B., Zhang, X., Xu, H., Zhao, J.X., 2022. U-Pb dating of oil charge in superimposed basins: a case study from the Tarim Basin, NW China. Geol. Soc. Am. Bull. 134 (11–12), 3176–3188.
Cherchi, A., Mancin, N., Montadert, L., Murru, M., Putzu, M.T., Schiavinotto, F., Verrubbi, V., 2008. The stratigraphic response to the Oligo-Miocene extension in the Western Mediterranean from observations on the Sardinia graben system (Italy). Bull. Soc. Geol. Fr. 179, 267–287.
Clauzon, G., Fleury, T.-J., Bellier, O., Molliex, S., Mocochain, L., Aguilar, J.-P., 2011. Morphostructural evolution of the luberon since the Miocene (SE France). Bull. Soc. Geol. Fr. 182, 95–110.
Cochard, J., Léonide, P., Borgomano, J., Guglielmi, Y., Massonnat, G., Rolando, J.P., et al., 2021. Reservoir properties of Barremian–Aptian urgonian limestones, SE France, part 2: influence of diagenesis and fracturing. J. Petrol. Geol. 44, 97–114.
Combes, P., 1984. La Tectonique Récente De La Provence Occidentale Microtectonique, Caractéristiques Dynamiques Et Cinématiques: Méthodologie De Zonation Tectonique Et Relations Avec La Séismicité. Université de Strasbourg, Strasbourg, France. Unpublished Ph.D. Thesis.
Combes, P.-J., 1990. Typologie, cadre géodynamique et genèse des bauxites françaises. Geodin. Acta 4, 91–109.
Cong, F., Tian, J., Hao, F., Kylander-Clark, A.R., Pan, W., Zhang, B., 2022. Calcite U-Pb ages constrain petroleum migration pathways in tectonic complex basins. Geology 50 (6), 644–649.
Corrêa, R.S.M., Ukar, E., Laubach, S.E., Aubert, I., Lamarche, J., Wang, Q., Stockli, D.F., Stockli, L.D., Larson, T.E., 2022. Episodic reactivation of carbonate fault zones with implications for permeability—an example from Provence, Southeast France. Mar. Petrol. Geol. 145, 105905.
Cruset, D., Cantarero, I., Vergés, J., John, C.M., Muñoz-López, D., Travé, A., 2018. Changes in fluid regime in syn-orogenic sediments during the growth of the south pyrenean fold and thrust. Global Planet. Change 171, 207–224.
Cruset, D., Vergés, J., Rodrigues, N., Belenguer, J., Pascual-Cebrian, E., Almar, Y., Pérez-Cáceres, I., Macchiavelli, C., Travé, A., Beranoaguirre, A., Albert, R., Gerdes, A.,

Messager, G., 2021. U–Pb dating of carbonate veins constraining timing of beef growth and oil generation within Vaca Muerta Formation and compression history in the Neuquén Basin along the Andean fold and thrust belt. Mar. Petrol. Geol. 132, 105204.
Cushing, E.M., Bellier, O., Nechtschein, S., Sébrier, M., Lomax, A., Volant, P., Dervin, P., Guignard, P., Bove, L.A., 2008. Multidisciplinary study of a slow-slipping fault for seismic hazard assessment: the example of the middle durance fault (SE France). Geophys. J. Int. 172, 1163–1178.
Daëron, M., 2021. Full propagation of analytical uncertainties in Δ_{47} measurements. G-cubed 22, e2020GC009592.
Daëron, M., Blamart, D., Peral, M., Affek, H.P., 2016. Absolute isotopic abundance ratios and the accuracy of Δ_{47} measurements. Chem. Geol. 442, 83–96.
Daëron, M., Vermeesch, P., 2024. Omnivariant generalized least squares regression: theory, geochronological applications, and making the case for reconciled Δ_{47} calibrations. Chem. Geol. 647, 121881.
Delacou, B., Sue, C., Champagnac, J.D., Burkhard, M., 2004. Present-day geodynamics in the bend of the western and central Alps as constrained by earthquake analysis. Geophys. J. Int. 158 (2), 753–774.
Dellisanti, F., Pini, G.A., Baudin, F., 2010. Use of Tmax as a thermal maturity indicator in orogenic successions and comparison with clay mineral evolution: relationship between T_{max} and clay minerals. Clay Miner. 45, 115–130.
Dercourt, J., Gaetani, M., Vrielynck, B., 2000. Atlas Peri-Tethys Palaeogeographical Maps. CCGM, Paris, France.
Dercourt, J., Zonenshain, L.P., Ricou, L.-E., Kazmin, V.G., Le Pichon, X., Knipper, A.L., Grandjacquet, C., Sbortshikov, I.M., Geyssant, J., Lepvrier, C., et al., 1986. Geological evolution of the tethys belt from the Atlantic to the pamirs since the liassic. Tectonophysics 123, 241–315.
Di Cuia, R., Gout, C., Balzagette, L., Masse, P., Vieban, F., 2005. Reservoir connectivity in a complex fractured reservoir: the relationship between fracturing and facies in the Upper Cretaceous Apulian Platform of the Maiella Mountain, Southern Italy. In: International Petroleum Technology Conference. IPTC-10817, IPTC.
Ebner, M., Koehn, D., Toussaint, R., Renard, F., Schmittbuhl, J., 2009. Stress sensitivity of stylolite morphology. Earth Planet Sci. Lett. 277, 394–398.
English, J.M., 2012. Thermomechanical origin of regional fracture systems. AAPG Bull. 96 (9), 1597–1625.
Espitalié, J., Burrus, J., 1986. Use of Tmax as a maturation index for different types of organic matter. Comparison with vitrinite reflectance. Thermal Modelling in Sedimentary Basins 11, 475–496.
Espitalié, J., Laporte, J.L., Madec, M., Marquis, F., Leplat, P., et al., 1977. Méthode rapide de caractérisation des roches mères, de leur potentiel pétrolier et de leur degré d'évolution. Oil Gas Sci. Technol. 32, 23–42.
Espurt, N., Hippolyte, J.-C., Saillard, M., Bellier, O., 2012. Geometry and kinematic evolution of a long-living foreland structure inferred from field data and cross section balancing, the sainte-victoire system, provence, France. Tectonics 31.
Evans, M.A., Fischer, M.P., 2012. On the distribution of fluids in folds: a review of controlling factors and processes. J. Struct. Geol. 44, 2–24.
Faccenna, C., Jolivet, L., Piromallo, C., Morelli, A., 2003. Subduction and the depth of convection in the Mediterranean mantle. J. Geophys. Res. Solid Earth 108.
Faccenna, C., Mattei, M., Funiciello, R., Jolivet, L., 1997. Styles of back-arc extension in the central Mediterranean. Terra Nova 9, 126–130.
Fattah, R., Salih, N., Préat, A., 2025. Direct dating of natural fracturing system in the Jurassic source rocks, NE Iraq: age constraint on multi fracture-filling cements and fractures associated with hydrocarbon phases/migration utilizing LA ICP MS. Minerals 15 (9), 907.
Gasparrini, M., Lacombe, O., Rohais, S., Belkacemi, M., Euzen, T., 2021. Natural mineralized fractures from the Montney-Doig unconventional reservoirs (Western Canada Sedimentary Basin) : timing and controlling factors. Mar. Petrol. Geol. 124, 104826.
Gasparrini, M., Mangenot, X., Bonifacie, M., Deschamps, P., Ceriani, A., 2025. Cooling and exhumation history of the Paris basin southeastern margin revealed by Δ47/U–Pb carbonate thermochronology. Terra Nova 37 (6), 421–430.
Gattacceca, J., Deino, A., Rizzo, R., Jones, D.S., Henry, B., Beaudoin, B., Vadeboin, F., 2007. Miocene rotation of Sardinia: new paleomagnetic and geochronological constraints and geodynamic implications. Earth Planet Sci. Lett. 258, 359–377.
Gaviglio, P., Gonzales, J.F., 1987. Fracturation et histoire tectonique du bassin de Gardanne (Bouches-Du-Rhone). Bull. Soc. Geol. Fr. III, 675–682.
Godeau, N., Deschamps, P., Guihou, A., Leonide, P., Tendil, A., Gerdes, A., Hamelin, B., Girard, J.-P., 2018. U-Pb dating of calcite cement and diagenetic history in microporous carbonate reservoirs: case of the Urgonian limestone, France. Geology 46, 247–250.
Grool, A.R., Ford, M., Vergès, J., Huismans, R.S., Christophoul, F., Dielforder, A., 2018. Insights into the crustal-scale dynamics of a doubly vergent orogen from a quantitative analysis of its forelands: a case study of the eastern Pyrenees. Tectonics 37, 450–476.
Gueguen, E., Doglioni, C., Fernandez, M., 1998. On the post-25 Ma geodynamic evolution of the western Mediterranean. Tectonophysics 298, 259–269.
Guieu, G., 1967. Un exemple de tectonique tangentielle; l'evolution du cadre montagneux de Marseille. Bull. Soc. Geol. Fr. S7-IX, 610–630.
Guieu, G., Roussel, J., 1990. Arguments for the pre-rift uplift and rift propagation in the Ligurian-Provencal Basin (northwestern Mediterranean) in the light of Pyrenean Provencal Orogeny. Tectonics 9 (5), 1113–1142.
Guignard, P., Bellier, O., Chardon, D., 2005. Géométrie et cinématique post-oligocène des failles d'Aix et de la moyenne Durance (Provence, France). C. R. Geosci. 337, 375–384.
Guyonnet-Benaize, C., 2011. Modélisation 3D Multi-Échelle Des Structures Géologiques De La Région De La Faille De La Moyenne Durance (SE France). Université Aix-Marseille, Marseille, France. Unpublished Ph.D. Thesis.
Guyonnet-Benaize, C., Lamarche, J., Hollender, F., Viseur, S., Münch, P., Borgomano, J., 2015. Three-dimensional structural modeling of an active fault zone based on complex outcrop and subsurface data: the middle Durance fault zone inherited from polyphase Meso-Cenozoic tectonics (Southeastern France). Tectonics 34, 265–289.
Guyonnet-Benaize, C., Lamarche, J., Masse, J.-P., Villeneuve, M., Viseur, S., 2010. 3D structural modelling of small-deformations in polyphase faults pattern. Application to the Mid-Cretaceous Durance Uplift, Provence (SE France). J. Geodyn. 50, 81–93.
Hemelsdaël, R., Séranne, M., Husson, E., Ballas, G., 2021. Structural style of the Languedoc Pyrenean thrust belt in relation with the inherited Mesozoic structures and with the rifting of the Gulf of Lion margin, southern France. Bull. Soc. Geol. Fr. 192, 46.
Hemingway, J.D., Henkes, G.A., 2021. A disordered kinetic model for clumped isotope bond reordering in carbonates. Earth Planet Sci. Lett. 566, 116962.
Hippolyte, J.-C., Angelier, J., Bergerat, F., Nury, D., Guieu, G., 1993. Tectonic-Stratigraphic record of paleostress time changes in the Oligocene basins of the Provence, Southern France. Tectonophysics 226, 15–35.
Hoareau, G., Crognier, N., Lacroix, B., Aubourg, C., Roberts, N.M.W., Niemi, N., Branellec, M., Beaudoin, N., Suárez Ruiz, I., 2021. Combination of Δ47 and U-Pb dating in tectonic calcite veins unravel the last pulses related to the Pyrenean shortening (Spain). Earth Planet Sci. Lett. 553, 116636.
Hooker, J.N., Gomez, L.A., Laubach, S.E., Gale, J.F.W., Marrett, R., 2012. Effects of diagenesis (cement precipitation) during fracture opening on fracture aperture-size scaling in carbonate rocks. In: Garland, J., Neilson, J.E., Laubach, S.E., Whidden, K.J. (Eds.), 370. Geological Society of London Special Publications. Advances in Carbonate Exploration and Reservoir Analysis.
Jakni, B., 2000. Thermochronologie Par Traces De Fission Des Marges Conjuguées Du Bassin liguro-provençal: La Corse Et Le Massif Des Maures-Tanneron. Université Joseph-Fourier - Grenoble I, p. 346p. Unpublished PhD thesis. https://theses.hal.science/tel-00644736v1.
Jiang, L., Wang, Z., Ou, Y., Ma, F., Wang, Y., 2025. Multiphase fracturing, fluid evolution, and geothermal sustainability in Mesoproterozoic carbonates of the north China craton. Basin Res. 37 (5), e70057.
Jolivet, L., Romagny, A., Gorini, C., Maillard, A., Thinon, I., Couëffé, R., et al., 2020. Fast dismantling of a mountain belt by mantle flow: Late-orogenic evolution of Pyrenees and Liguro-Provençal rifting. Tectonophysics 776, 228312.
Kaci, Tassadit, 2019. Analyse De La Sequence De Déformation Dans Le Pli De Mirabeau (SE France). Aix-Marseille Université, p. 35p. Unpublished Master thesis.
Kim, S.-T., O'neil, J.R., 1997. Equilibrium and nonequilibrium oxygen isotope effects in synthetic carbonates. Geochem. Cosmochim. Acta 61, 3461–3475.
Kim, S.-T., O'Neil, J.R., Hillaire-Marcel, C., Mucci, A., 2007. Oxygen isotope fractionation between synthetic aragonite and water: influence of temperature and Mg2+ concentration. Geochem. Cosmochim. Acta 71, 4704–4715.
Koehn, D., Ebner, M., Renard, F., Toussaint, R., Passchier, C.W., 2012. Modelling of stylolite geometries and stress scaling. Earth Planet Sci. Lett. 341, 104–113.
Koehn, D., Köehler, S., Toussaint, R., Ghani, I., Stollhofen, H., 2022. Scaling analysis, correlation length and compaction estimates of natural and simulated stylolites. Journal of Structural Geolology 161, 104670.
Koehn, D., Renard, F., Toussaint, R., Passchier, C., 2007. Growth of stylolite teeth patterns depending on normal stress and finite compaction. Earth Planet Sci. Lett. 257, 582–595.
Koehn, D., Rood, M.P., Beaudoin, N., Chung, P., Bons, P.D., Gomez-Rivas, E., 2016. A new stylolite classification scheme to estimate compaction and local permeability variations. Sediment. Geol. 346, 60–71.
La Bruna, V., Lamarche, J., Agosta, F., Rustichelli, A., Giuffrida, A., Salardon, R., Marié, L., 2020. Structural diagenesis of shallow platform carbonates: role of early embrittlement on fracture setting and distribution, case study of Monte Alpi (Southern Apennines, Italy). J. Struct. Geol. 131, 103940.
Labeur, A., Beaudoin, N., Lacombe, O., Emmanuel, L., Petracchini, L., Daëron, M., Klimowicz, S., Callot, J.P., 2021. Burial-deformation history of folded rocks unraveled by fracture analysis, stylolite paleopiezometry and vein cement geochemistry: a case study in the Cingoli Anticline (Umbria-Marche, northern Apennines). Geosciences 11, 135.
Labeur, A., Beaudoin, N.E., Lacombe, O., Gout, G., Callot, J.P., 2024. Constraining the onset of orogenic contraction in fold-and-thrust belts using sedimentary stylolite populations (Umbria-Marche Apennines, Italy). J. Struct. Geol. 182, 105098.
Lacombe, O., Angelier, J., Laurent, P., 2012. Determining paleostress orientations from faults and calcite twins: a case study near the Sainte-Victoire Range (Southern France). Tectonophysics 201, 141–156, 1992.
Lacombe, O., Beaudoin, N.E., 2024. Timing, sequence, duration and rate of deformation in fold-and-thrust belts: a review of traditional approaches and recent advances from absolute dating (K–Ar Illite/U–Pb Calcite) of brittle structures. C. R. Geosci. 356, 467–494.
Lacombe, O., Beaudoin, N.E., Hoareau, G., Labeur, A., Pecheyran, C., Callot, J.-P., 2021. Dating folding beyond folding, from layer-parallel shortening to fold tightening, using mesostructures: lessons from the Apennines, Pyrenees, and Rocky Mountains. Solid Earth 12, 2145–2157.
Lacombe, O., Jolivet, L., 2005. Structural and kinematic relationships between corsica and the pyrenees-provence domain at the time of the Pyrenean orogeny. Tectonics 24, TC1003.
Lacombe, O., Rolland, Y., 2016. Special issue: "Fluids in crustal deformation: fluid flow, fluid-rock interactions, rheology, melting and resources". J. Geodyn. 101, 1–4.

Lacombe, O., Tavani, S., Lamarche, J., Balsamo, F., Agosta, F., 2022. Special issue: "Faults and fractures in rocks: mechanics, occurrence, dating, stress history and fluid flow". Geol. Mag. 159 (11–12), 1847–1854.
Lamarche, J., Kaci, T., Marié, L., Richard, P., 2020. Fracture sequence in folded carbonates: a long and complex history of reservoir properties. In: 4th EAGE Workshop on Naturally Fractured Reservoirs. European Association of Geoscientists & Engineers (EAGE), pp. 11–13. February 2020, Ras Al Khaimah, United Arab Emirates.
Lamarche, J., Lavenu, A.P.C., Gauthier, B.D.M., Guglielmi, Y., Jayet, O., 2012. Relationships between fracture patterns, geodynamics and mechanical stratigraphy in Carbonates (South-East Basin, France). Tectonophysics 581, 231–245.
Laubach, S.E., Eichhubl, P., Hilgers, C., Lander, R.H., 2010. Structural diagenesis. J. Struct. Geol. 32, 1866–1872.
Laubach, S.E., Lander, R.H., Criscenti, L.J., Anovitz, L.M., Urai, J.L., Pollyea, R.M., Hooker, J.N., Narr, W., Evans, M.A., Kerisit, S.N., Olson, J.E., Dewers, T., Fisher, D., Bodnar, R., Evans, B., Dove, P., Bonnell, L.M., Marder, M.P., Pyrak-Nolte, L., 2019. The role of chemistry in fracture pattern development and opportunities to advance interpretations of geological materials. Rev. Geophys. 57, 1065–1111.
Lavenu, A.P.C., Lamarche, J., 2018. What controls diffuse fractures in platform carbonates? Insights from Provence (France) and Apulia (Italy). J. Struct. Geol. 108, 94–107.
Lavenu, A.P.C., Lamarche, J., Gallois, A., Gauthier, B.D.M., 2013. Tectonic versus diagenetic origin of fractures in a naturally fractured carbonate reservoir analog (Nerthe anticline, southeastern France). AAPG (Am. Assoc. Pet. Geol.) Bull. 97 (12), 2207–2232.
Lavenu, A.P.C., Lamarche, J., Salardon, R., Gallois, A., Marié, L., Gauthier, B.D.M., 2014. Relating background fractures to diagenesis and rock physical properties in a platform–slope transect. Example of the Maiella Mountain (central Italy). Mar. Petrol. Geol. 51, 2–19.
Leleu, S., Ghienne, J.-F., Manatschal, G., 2009. Alluvial fan development and morpho-tectonic evolution in response to contractional fault reactivation (late Cretaceous–Palaeocene), Provence, France. Basin Res. 21 (2), 157–187.
Léonide, P., Floquet, M., Villier, L., 2007. Interaction of tectonics, eustasy, climate and carbonate production on the sedimentary evolution of an early/middle Jurassic extensional basin (Southern Provence Sub-basin, SE France). Basin Res. 19 (1), 125–152.
Léonide, P., Fournier, F., Reijmer, J.J., Vonhof, H., Borgomano, J., Dijk, J., Rosenthal, M., van Goethem, M., Cochard, J., Meulenaars, K., 2014. Diagenetic patterns and pore space distribution along a platform to outer-shelf transect (Urgonian limestone, Barremian–Aptian, SE France). Sediment. Geol. 306, 1–23.
MacDonald, J.M., Faithfull, J.W., Roberts, N.M.W., Davies, A.J., Holdsworth, C.M., Newton, M., Williamson, S., Boyce, A., John, C.M., 2019. Clumped-isotope palaeothermometry and LA-ICP-MS U–Pb dating of lava-pile hydrothermal calcite veins. Contrib. Mineral. Petrol. 174 (7), 63.
MacDonald, J.M., VanderWal, J., Roberts, N.M.W., Winkelstern, I.Z., Faithfull, J.W., Boyce, A.J., 2024. Fingerprinting fluid source in calcite veins: combining LA-ICP-MS U-Pb calcite dating with trace elements and clumped isotope palaeothermometry. Tektonika 2 (1), 27–39.
Mangenot, X., Bonifacie, M., Gasparrini, M., Götz, A., Chaduteau, C., Ader, M., Rouchon, V., 2017. Coupling Δ47 and fluid inclusion thermometry on carbonate cements to precisely reconstruct the temperature, salinity and δ18O of paleo-groundwater in sedimentary basins. Chem. Geol. 472, 44–57.
Mangenot, X., Gasparrini, M., Gerdes, A., Bonifacie, M., Rouchon, V., 2018. An emerging thermochronometer for carbonate-bearing rocks: Δ47/(U-Pb). Geology 46 (12), 1067–1070.
Manniello, C., Agosta, F., Todaro, S., Cavalcante, F., Prosser, G., 2022. Fracture stratigraphy of Mesozoic platform carbonates, Agri Valley, southern Italy. Geol. Mag. 159 (11–12), 1874–1896.
Masse, J., Philip, J., 1976. Paléogéographie et tectonique du Crétacé moyen en Provence: révision du concept d'isthme durancien. Rev. Géogr. Phys. Géol. Dyn. 18, 49–66.
Masse, J.-P., Villeneuve, M., Leonforte, E., Nizou, J., 2009. Block tilting of the North Provence Early Cretaceous carbonate margin: stratigraphic, sedimentologic and tectonic data. Bull. Soc. Geol. Fr. 180, 105–115.
Matonti, C., Lamarche, J., Guglielmi, Y., Marié, L., 2012. Structural and petrophysical characterization of mixed conduit/seal fault zones in carbonates: example from the Castellas fault (SE France). J. Struct. Geol. 39, 103–121.
McArthur, J.M., Howarth, R.J., Shields, G.A., 2012. Strontium isotope stratigraphy. In: The Geologic Time Scale. Elsevier, pp. 127–144. https://doi.org/10.1016/B978-0-444-59425-9.00007-X.
Molliex, S., 2009. Caractérisation De La Déformation Tectonique Récente En Provence (SE France). Université Paul Cézanne-Aix-Marseille III, Marseille, France. Unpublished Ph.D. Thesis.
Molliex, S., Bellier, O., Terrier, M., Lamarche, J., Martelet, G., Espurt, N., 2011. Tectonic and sedimentary inheritance on the structural framework of Provence (SE France): importance of the Salon-Cavaillon fault. Tectonophysics 501, 1–16.
Mondillo, N., Chelle-Michou, C., Putzolu, F., Balassone, G., Mormone, A., Santoro, L., Cretella, S., Scognamiglio, G., Tarallo, M., Tavani, S., 2025. The mid-cretaceous Bauxites of SE France: Geochemistry, U-Pb Zircon dating and their implications for the paleogeography at the junction between Alpine Tethys and pyrenean rift. Gondwana Res. 137, 145–170.
Morillon, A.C., 1997. Etude thermo-chronométrique Appliquée Aux Exhumations En Contexte Orogénique: Le Massif Des Maures (France) Et Les Cordillères Bétiques (Espagne). Unpublished PhD thesis, Nice.
Moss, S., Tucker, M.E., 1995. Diagenesis of Barremian-Aptian platform carbonates (the Urgonian limestone Formation of SE France): near-surface and shallow-burial diagenesis. Sedimentology 42 (6), 853–874.
Mouthereau, F., Filleaudeau, P.-Y., Vacherat, A., Pik, R., Lacombe, O., Fellin, M.G., Castelltort, S., Christophoul, F., Masini, E., 2014. Placing limits to shortening evolution in the Pyrenees: role of margin architecture and implications for the Iberia/Europe convergence. Tectonics 33, 2283–2314.
Muñoz-López, D., Cruset, D., Vergés, J., Cantarero, I., Benedicto, A., Mangenot, X., Albert, R., Gerdes, A., Beranoaguirre, A., Travé, A., 2022. Spatio-temporal variation of fluid flow behavior along a fold: the Boixols-Sant Corneli anticline (Southern Pyrenees) from U–Pb dating and structural, petrographic and geochemical constraints. Mar. Petrol. Geol. 143, 105788.
Naeser, N.D., McCulloh, T.H. (Eds.), 2012. Thermal History of Sedimentary Basins: Methods and Case Histories. Springer Science & Business Media.
Ni, R., Chen, Y., Song, Y., Zhang, H., Feng, Y., Hao, F., Lu, X., Ma, X., 2025. Reconstructing hydrocarbon accumulation and burial history of Permian reservoirs in northwest Sichuan Basin, China: integrated fluid inclusion thermometry and U-Pb dating. Mar. Petrol. Geol., 107539
Olivet, J.-L., 1996. La Cinématique de la Plaque Ibérique. Bulletin des Centres de Recherche et Exploration-Production Elf-Aquitaine 20, 131–195.
Petit, J.-P., Mattauer, M., 1995. Palaeostress superimposition deduced from mesoscale structures in limestone: the Matelles exposure, Languedoc, France. J. Struct. Geol. 17 (2), 245–256.
Petit, J.P., Chemenda, A.I., Minisini, D., Richard, P., Bergman, S.C., Gross, M., 2022. When do fractures initiate during the geological history of a sedimentary basin? Test case of a loading-fracturing path methodology. J. Struct. Geol. 164, 104683.
Petrie, E.S., Jeppson, T.N., Evans, J.P., 2012. Predicting rock strength variability across stratigraphic interfaces in caprock lithologies at depth: correlation between outcrop and subsurface. Environ. Geosci. 19 (4), 125–142.
Philip, J., 1972. Palaeoécologie des Formations à Rudistes du Crétacé Supérieur - l'exemple du Sud-Est de la France. Palaeogeogr. Palaeoclimatol. Palaeoecol. 12, 205–222.
Pin, C., Zalduegui, J.S., 1997. Sequential separation of light rare-earth elements, thorium and uranium by miniaturized extraction chromatography: application to isotopic analyses of silicate rocks. Anal. Chim. Acta 339 (1–2), 79–89.
Pironon, J., Bourdet, J., 2008. Petroleum and aqueous inclusions from deeply buried reservoirs: Experimental simulations and consequences for overpressure estimates. Geochim. Cosmochim. Acta 72 (20), 4916–4928.
Regnet, J.B., David, C., Robion, P., Menendez, B., 2019. Microstructures and physical properties in carbonate rocks: a comprehensive review. Mar. Petrol. Geol. 103, 366–376.
Rispoli, R., 1981. Stress fields about strike-slip faults inferred from stylolites and tension gashes. Tectonophysics 75 (3–4), 29–36.
Rolland, A., Toussaint, R., Baud, P., Conil, N., Landrein, P., 2014. Morphological analysis of stylolites for paleostress estimation in limestones. Int. J. Rock Mech. Min. Sci. 67, 212–225.
Rosenbaum, G., Lister, G., Duboz, C., 2002. Reconstruction of the tectonic evolution of the Western Mediterranean since the Oligocene. J. Virtual Explor. 8, 107–130.
Roure, F., Andriessen, P., Callot, J.-P., Ferket, H., Gonzalez, E., Guilhaumou, N., Hardebol, N., Lacombe, O., Malandain, J., Mougin, P., Muska, K., Ortuno, S., Sassi, W., Swennen, R., Vilasi, N., 2010. The use of paleo-thermo-barometers and coupled thermal, fluid flow and pore fluid pressure modelling for hydrocarbon and reservoir prediction in fold-and-thrust belts. "Hydrocarbons in Contractional Belts" 348, 87–114. Geological Society of London, Special Publications.
Roure, F., Colletta, B., 1996. Cenozoic inversion structures in the foreland of the Pyrenees and Alps. Cenozoic Inversion Structures in the Foreland of the Pyrenees and Alps Mémoires du Muséum National d'Histoire Naturelle 170, 173–209.
Salih, N., Mansurbeg, H., Kolo, K., Gerdes, A., Préat, A., 2019. In situ U-Pb dating of hydrothermal diagenesis in tectonically controlled fracturing in the Upper Cretaceous Bekhme Formation, Kurdistan Region-Iraq. Int. Geol. Rev. 62, 2261–2279.
Saspiturry, N., Lahfid, A., Baudin, T., Guillou-Frottier, L., Razin, P., Issautier, B., Le Bayon, B., Serrano, O., Lagabrielle, Y., Corre, B., 2020. Paleogeothermal gradients across an inverted hyperextended rift system: example of the Mauleon Fossil Rift (Western Pyrenees). Tectonics 39 (10), e2020TC006206.
Sassi, W., Guiton, M.L.E., Leroy, Y.M., Daniel, J.-M., Callot, J.-P., 2012. Constraints on bed scale fracture chronology with a FEM mechanical model of folding: the case of Split Mountain (Utah, USA). Tectonophysics 576–577, 197–215.
Schettino, A., Turco, E., 2011. Tectonic history of the western Tethys since the late Triassic. Geol. Soc. Am. Bull. 123, 89–105.
Schmittbuhl, J., Renard, F., Gratier, J.P., Toussaint, R., 2004. Roughness of stylolites: implications of 3D high resolution topography measurements. Phys. Rev. Lett. 93, 238501.
Séranne, M., 1999. The Gulf of Lion Continental Margin (NW Mediterranean) Revisited by IBS: an Overview, 156. Geological Society of London Special Publications, pp. 15–36.
Séranne, M., Benedicto, A., Labaume, P., Truffert, C., Pascal, G., 1995. Structural style and evolution of the Gulf of Lion Oligo-Miocene rifting: role of the Pyrenean orogeny. Mar. Petrol. Geol. 12, 809–820.
Séranne, M., Couëffé, R., Husson, E., Baral, C., Villard, J., 2021. The transition from Pyrenean shortening to Gulf of Lion rifting in Languedoc (South France). A tectonic-sedimentation analysis. Bull. Soc. Geol. Fr. 192, 27.
Simonsen, I., Hansen, A., Nes, O.M., 1998. Determination of the Hurst exponent by use of wavelet transforms. Phys. Rev. 58, 2779–2787.
Smeraglia, L., Fabbri, O., Choulet, F., Buatier, M., Boulvais, P., Bernasconi, S.M., Castorina, F., 2020. Syntectonic fluid flow and deformation mechanisms within the frontal thrust of a foreland fold-and-thrust belt: example from the Internal Jura, Eastern France. Tectonophysics 778, 228178.

Stockdale, P.B., 1922. Stylolites: Their Nature and Origin. Indiana University, p. 97. Unpublished PhD thesis.
Su, A., Chen, H., Feng, Y.X., Zhao, J.X., 2022. LA-ICP-MS U-Pb dating and geochemical characterization of oil inclusion-bearing calcite cements: constraints on primary oil migration in lacustrine mudstone source rocks. Geol. Soc. Am. Bull. 134 (7–8), 2022–2036.
Tavani, S., Bertok, C., Granado, P., Piana, F., Salas, R., Vigna, B., Muñoz, J.A., 2018. The Iberia-Eurasia plate boundary east of the Pyrenees. Earth Sci. Rev. 187, 314–337.
Tavani, S., Storti, F., Lacombe, O., Corradetti, A., Muñoz, J.A., Mazzoli, S., 2015. A review of deformation pattern templates in foreland basin systems and fold-and-thrust belts: implications for the state of stress in the frontal regions of thrust wedges. Earth Sci. Rev. 141, 82–104.
Tempier, C., 1987. Modèle nouveau de mise en place des structures provencales. Bull. Soc. Geol. Fr. III, 533–540.
Tempier, C., Durand, J., 1981. Importance de l'épisode Tectonique d'âge Crétacé Supérieur dans la Structure du Versant Méridional de la Montagne Sainte-Victoire (Provence). Comptes Rendus de l'Académie des Sciences Paris 293, 629–632.
Tissot, B.P., Pelet, R., Ungerer, P.H., 1987. Thermal history of sedimentary basins, maturation indices, and kinetics of oil and gas generation. AAPG (Am. Assoc. Pet. Geol.) Bull. 71 (12), 1445–1466.
Toussaint, R., Aharonov, E., Koehn, D., Gratier, J.P., Ebner, M., Baud, P., Rolland, A., Renard, F., 2018. Stylolites: a review. J. Struct. Geol. 114, 163–195.
van Hinsbergen, D.J.J., Torsvik, T.H., Schmid, S.M., Maţenco, L.C., Maffione, M., Vissers, R.L.M., Gürer, D., Spakman, W., 2020. Orogenic architecture of the Mediterranean region and kinematic reconstruction of its tectonic evolution since the Triassic. Gondwana Res. 81, 79–229.
Vergés, J., Fernandez, M., Martìnez, A., 2002. The Pyrenean orogen: pre-, syn-, and post-collisional evolution. J. Virtual Explor. 8. https://doi.org/10.3809/jvirtex.2002.00058.
Villeger, M., 1984. Évolution Tectonique Du Panneau De Couverture nord-provençal (Mont Ventoux, Luberon, Moyenne Durance), France. Université Paris Sud-Paris XI. Unpublished PhD thesis.
Vitale, S., Dati, F., Mazzoli, S., Ciarcia, S., Guerriero, V., Iannace, A., 2012. Modes and timing of fracture network development in poly-deformed carbonate reservoir analogues, mt. Chianello, southern Italy. J. Struct. Geol. 37, 223–235.
Wright, K., Cygan, R.T., Slater, B., 2001. Structure of the (1014) surfaces of calcite, dolomite and magnesite under wet and dry conditions. Phys. Chem. Chem. Phys. 3, 839–844.
Yalcin, M.N., Littke, R., Sachsenhofer, R.F., 1997. Thermal history of sedimentary basins. In: Petroleum and Basin Evolution: Insights from Petroleum Geochemistry, Geology and Basin Modeling. Springer Berlin Heidelberg, Berlin, Heidelberg, pp. 71–167.
Yuan, F., Tian, J., Hao, F., Liu, Z., Zhang, K., Wang, X., 2024. Fault characterization and its significance on hydrocarbon migration and accumulation of western Tazhong Uplift, Tarim Basin: insight from seismic, geochemistry, fluid inclusion and in situ U-Pb dating. Mar. Petrol. Geol. 170, 107137.
Zeboudj, A., Bah, B., Lacombe, O., Beaudoin, N.E., Gout, C., Godeau, N., Girard, J.-P., Deschamps, P., 2023. Depicting past stress history at passive margins: a combination of calcite twinning and stylolite roughness paleopiezometry in supra-salt sendji deep carbonates, lower Congo Basin,West Africa. Mar. Petrol. Geol. 152, 106219.
Zeboudj, A., Lacombe, O., Beaudoin, N.E., Callot, J.P., Lamarche, J., Guihou, A., Hoareau, G., 2025a. Sequence, duration, rate of deformation and paleostress evolution during fold development : insights from fractures, calcite twins and U-Pb calcite geochronology in the Mirabeau anticline (SE France). J. Struct. Geol. 199, 105460, 356, S2.
Zeboudj, A., Lacombe, O., Beaudoin, N.E., Callot, J.P., Lamarche, J., Guihou, A., Hoareau, G., Barbotin, G., Pecheyran, C., Deschamps, P., 2025b. Timing of deformation in the Provence fold-and-thrust belt (SE France) as constrained by U-Pb calcite geochronology. Geosciences 15, 463.
Zhang, C., Wen, H., Wang, X., Wen, L., Shen, A., Zhou, G., Wang, Q., She, M., Ma, C., Quiao, Z., Liu, D., Ma, Y., 2024. Formational stages of natural fractures revealed by U-Pb dating and CO-Sr-Nd isotopes of dolomites in the Ediacaran Dengying Formation, Sichuan Basin, southwest China. Geol. Soc. Am. Bull. 136 (11–12), 4671–4688.